INVESTIGATION OF REAL GAS EFFECTS ON CENTRIFUGAL COMPRESSOR ANALYTICAL METHODS FOR SUPERCRITICAL CO_2 POWER CYCLES

by

LAUREN ALEXANDRA BLANCHETTE
B.S.M.E., University of Central Florida, Orlando, 2014

A thesis submitted in partial fulfillment of the requirements
for the degree of Master of Science in Mechanical Engineering
in the Department of Mechanical and Aerospace Engineering
in the College of Engineering and Computer Science
at the University of Central Florida
Orlando, Florida

Fall Term
2016

Major Professor: Jayanta Kapat

ABSTRACT

As supercritical carbon dioxide (sCO_2) power cycles have shown potential to be the next generation power cycle, an immense amount of research has gone into developing this system. One of the setbacks facing development and optimization of this cycle is the unknown in current design and analysis methods ability to accurately model turbomachinery working with sCO_2. Due to the desired inlet conditions to the compressor close proximity to the critical point, accurate design and analysis of this power cycle component is one of the main concerns. The present study provides aerodynamic analysis of a centrifugal compressor impeller blade with sCO_2 as the working fluid through a comparative study between three dimensional (3D) computational fluid dynamics (CFD) and a one dimensional (1D) mean line analyses. The main centrifugal compressor in reference to a 100 MW sCO_2 closed loop Recuperated Recompression Brayton cycle is investigated. Through the use of conventional loss correlations for centrifugal compressors found in the literature, and geometrical parameters developed through a past mean line design, losses were calculated for the specified compressor impeller. The aerodynamic performance is then predicted through the 1D analysis. Furthermore, the boundary conditions for the CFD analysis were derived through the mean line analysis of the centrifugal compressor to carry out the 3D study of the sCO_2 impeller blade. As the Span and Wagner equation of state has been proven to be the most accurate when working in the vicinity of the critical point, this real gas equation of state was implemented in both analyses. Consequently, a better understanding was developed on best practices for modeling a real gas sCO_2 centrifugal compressor along with the limitations that currently exist when utilizing commercial CFD solvers. Furthermore, the resulting performance and aerodynamic behavior from the 1D analysis were compared with the predicted conclusions

from the CFD analysis. Past literature studies on sCO_2 compressor analysis methodology have been focused on small scale power cycles. This work served as the first comparison of 1D and 3D analysis methodology for large scale sCO_2 centrifugal compressors.

The lack of commercial CFD codes able to model phase change within sCO_2 turbomachinery and the possible breach of flow properties into the saturation region at the leading edge of the impeller blade creates a limit to the operating conditions that can be simulated within these analysis tools. Further, the rapid expansion rate within this region has been predicted to cause non-equilibrium condensation leading the fluid to a metastable vapor state. Due to the complexity of two phase models, a proposed methodology to model sCO_2 compressors as single phase is to represent metastable properties through the extrapolation of equilibrium properties onto the liquid domain up until the spinodal limit. This equation of state definition with metastable properties was used to model a 3D converging-diverging nozzle due to the similar flow dynamics occurring when compared to a compressor blade channel. The equation of state was implemented through a temperature and pressure dependent property table amended with metastable properties using the NIST REFPROP Database. Modeling was performed for inlet conditions with varied closeness to the fluid's critical point. Investigation on the accuracy of utilizing this table to define sCO_2 properties with respect to its resolution was executed. Through this, it was determined that the resulting interpolation error was highly influenced on the closeness to the critical point. Additionally, the effect on the capable modeling operating region when utilizing the metastable real gas property table through single phase modeling was examined.

This work is dedicated to my family and Taylor Benton

for their unconditional love and support

ACKNOWLEDGMENTS

Thank you to everyone at the CATER lab that has helped me reach this point in anyway, whether it was directly related to my research or just through

everyday encouragement and a friendly face.

I further want to express my gratitude to my undergraduate advisor, Dr. Kassab and my graduate advisor, Dr. Kapat for providing me with the unique opportunities that I collaborated on throughout my time at UCF.

The experiences with all of you have shaped what it means for me to be an engineer with incredible passion for my work.

TABLE OF CONTENTS

LIST OF FIGURES

LIST OF TABLES

NOMENCLATURE

Ω	Rotation Speed, 1/s
ω	Internal Loss coefficient
λ	Impeller Tip Distortion Factor
β	Blade Angle
β'	Relative Flow Angle
δ_{TCL}	Tip Clearance Gap, m
ρ	Density, kg/m^3
η	Efficiency
μ	Dynamic Viscosity, kg/μm-s
a	Speed of Sound, m/s
b	Blade height, m
B	Area Blockage
C	Flow Absolute Velocity, m/s
Cp	Isobaric Specific Heat Capacity, kJ/kg-K
Cv	Isochoric Specific Heat Capacity, kJ/kg-K
D_f	Diffusion Factor
D_h	Hydraulic Diameter, m
e_a	Approximate Relative Error
e_{ext}	Extrapolated Relative Error
h	Specific Enthalpy, kJ/kg

I_B	Blade Work Input Coefficients
k	Thermal Conductivity, kW/m-K
k_m	Streamline Curvature
L	Blade Mean Streamline Meridional Length, m
ṁ	Mass Flow Rate, kg/s
$\dot{m}_{CL}$	Blade Tip Gap Leakage Mass Flow Rate, kg/s
P	Pressure, MPa
r	Radius, m
s	Specific Entropy, kJ/kg
T	Temperature, K
t	Blade Thickness, m
U	Blade Speed, m/s
V	Flow Relative Velocity, m/s
V_{CL}	Velocity of tip gap clearance flow, m/s
ΔZ	Axial Length of Impeller, m
Z	Number of Blades in the Impeller

SUBSCRIPTS

0	Total or Stagnation state
1	Impeller Inlet
2	Impeller Exit
3	Vaneless Diffuser Exit
θ	Tangential Component
AMC	Acceleration Margin to Condensation
cp	Critical Point
m	Meridional Component
r	Radial component
R	Thermodynamic State in the Relative Frame
S	Value at Ideal State
t	Impeller Tip
tt	Total-to-Total
v	Vapor
s	Saturation
z	Axial component

ABBREVIATIONS

1D	One-Dimensional
3D	Three-Dimensional
AMC	Acceleration Margin to Condensation
CAD	Computer Aided Design
CATER	Center for Advanced Turbomachinery and Energy Research
CD	Converging-Diverging
CFD	Computational Fluid Dynamics
CSP	Concentrated Solar Power
EOS	Equation of State
GCI	Grid Convergence Index
HTF	Heat Transfer Fluid
RANS	Reynolds Averaged Navier-Stokes
RGP	Real Gas Property
sCO_2	Supercritical Carbon Dioxide
SNL	Sandia National Laboratory
TIT	Turbine Inlet Temperature

CHAPTER 1: INTRODUCTION

1.1 Background and Motivation

As energy production and use are by far the largest man-made sources of air pollutants [1], the power generation industry is currently facing the rising demand for energy while simultaneously needing to lower the amount of harmful greenhouse gas emissions being released. With the objective of economically reducing air pollutants released in the future, it is becoming vital to find alternative sustainable energy resources. World Energy Outlook 2015 proclaims "Annual investment in low-carbon technologies in our central scenario is increasing, but the cumulative $7.4 trillion invested in renewable energy to 2040 represents only around 15% of total investment in global energy supply" [2]. Furthermore, even with the increasing interest in sustainable energy resources, it is still predicted that coal and natural gas will be the leading source of electricity generated by 2040 (Figure 1) [3]. In order to increase the total investment in low-carbon technologies even further, it is essential to create economically competitive solutions compared to the leading energy sources, now coal and natural gas [3].

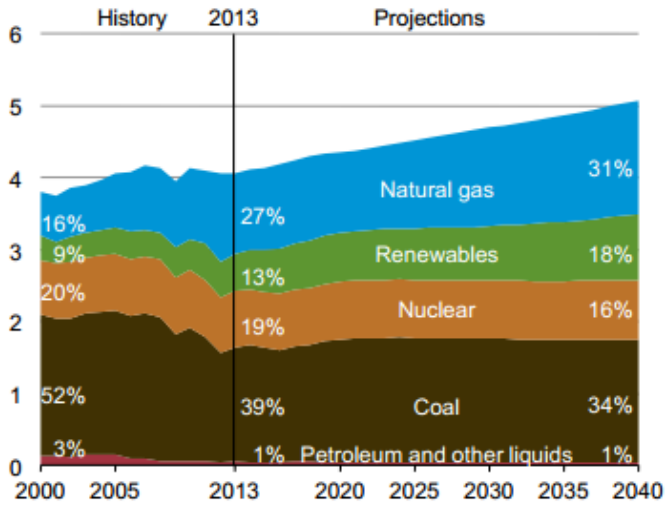

Figure 1: Electricity Generation by Fuel, 2000-2040 (trillion kilowatt-hours) [3]

One such way researchers are attempting to meet this objective is by utilizing alternative fluids for power generation cycles, such as supercritical carbon dioxide (sCO_2) and helium. Although the idea of utilizing sCO_2 as the working fluid in power cycles first came about in 1967, it took the work of Dostal [4] in 2004 to revitalize the idea through displaying the cycle's economic and efficiency benefits, among others, for nuclear reactor applications. As such, the amount of research collaboration around the world from academia, industry, and national and independent laboratories to develop this cycle has increased tremendously.

Due to the high density of sCO_2, the cycle components size is estimated to be relatively small compared to conventional power cycles (Figure 2). Utilizing sCO_2 also shows increase in efficiency and lower back-work ratio when compared to its competing working fluids. SCO_2 Brayton cycles with recompression have the potential to reach a higher efficiency and a simpler more compact power block than superheated steam cycle [5].

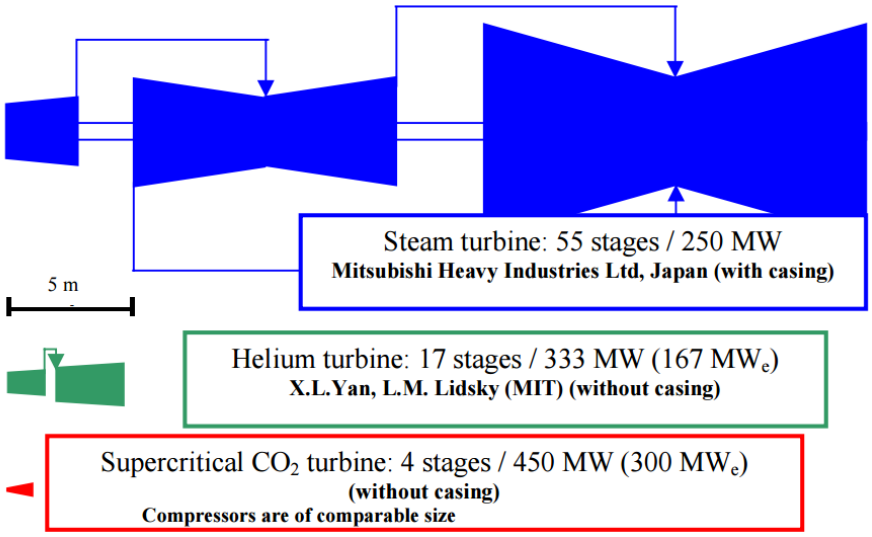

Figure 2: Comparison of Turbine Sizes for Steam, Helium, and CO2 [4]

With its inherent benefits and broad operational temperature range, employing sCO_2 as the working fluid in power generation cycles has shown immense potential in multiple applications, such as concentrated solar power (CSP), waste heat recovery (WHR), nuclear reactors, and replacement of steam cycles in combined cycle power plants (Figure 3).

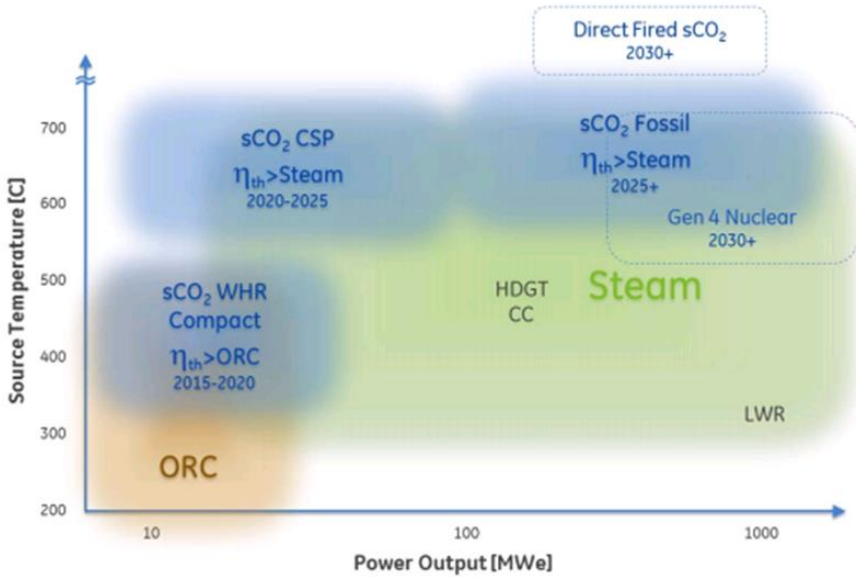

Figure 3: Application Space for sCO_2 Power Cycles [6]

The U.S. Department of Energy has invested in many projects to further develop this power cycle. One in particular is the SunShot Initiative, in which the objective is to make solar energy cost-competitive with the other leading forms of electricity by the end of this decade. One such way that researchers are seeking to meet this objective is through reducing the cost of Concentrated Solar Power (CSP) systems. These systems entail a heliostat field, solar receiver, and a power conversion system. Utilizing sCO_2 Brayton cycles as the power conversion system operating at a relatively high turbine inlet temperature (TIT) has been recognized as the most promising technology capable of attaining SunShots' cost and performance objectives for the power block [7]. With this being known, the initiative has turned towards integrating this cycle into the CSP power block and moving it forward to commercial use.

Furthermore, the work at the Center for Advanced Turbomachinery and Energy Research (CATER) has dedicated their efforts to aid in the development of sCO_2 Brayton Power cycles through cycle optimization, and design and analysis of different cycle components, such as the heat exchanger, axial turbine, and centrifugal compressors. Within this process, technology has to be further developed and design methods have to be altered for each component to be tailored towards the unconventional fluid sCO_2. Many unknowns such as how this fluid functions within these operating conditions and the fluid dynamic differences between ideal need to further be assessed for the accuracy of the modeling methodologies used.

1.2 Challenges

While the potential of sCO_2 power cycles has become widely known, there are still many components that need to be further understood and optimally designed for this working fluid before

this cycle can go full force into the energy industry. Some of these unknowns currently under investigation include the following: the performance of the turbomachinery components, current bearing and seal technology capable of withstanding the high operating pressure of sCO_2, and the development of economic, compact heat exchangers. SCO_2 power cycles operate under stark conditions, such as high rotational speeds and high fluid density and pressure. These harsh conditions have created some technical concerns on bearing stability and seal technology that need to be addressed for successful operation near the sCO_2 critical point (304.128 K and 7.377 MPa).

Another challenge, specifically with CSP applications, is developing a heat transfer fluid that can produce a higher temperature at the inlet to the turbine and ultimately increase the efficiency. Currently, the TIT produced by using conventional heat transfer fluids (HTF), such as molten salt is around 565 Celsius. This is a challenge that must be overcome to further reduce the capitol cost and increase the efficiencies of the power conversion systems. Directly using sCO_2 as the HTF and the working fluid within the power cycle eliminates the heat exchanger between the working fluid and the HTF and has potential to increase the TIT to much higher temperatures than what is currently seen within CSP technology. This is a relatively new idea therefore there are still an abundance of difficulties that need to be addressed.

Although there is a tremendous amount of ways to further develop this cycle and its applications, this work focuses on the challenges with modeling of the compressor. As accurate modeling of the compressor is an important stage in the design process, this topic is imperative to investigate. Douglas [6] displays the development of accurate modeling tools as being one of the current technology gaps to developing a high temperature sCO_2 power cycle pilot test loop, an important step in creating a demo of this innovative power cycle.

Further development of 1D analysis to be tailored specifically to sCO_2 turbomachinery is a key to accurate loss calculations, as current conventional loss models are used and losses associated with condensation are not yet considered. The large fluctuations in thermodynamic properties such as specific heat when approaching the critical point bring about uncertainties in the applicability of loss models developed through conventional fluid experiments to sCO_2 turbomachinery, specifically for the compressor. Due to the lack of experimental research, this becomes an intricate process. In addition to the conventional losses that need to be re-evaluated for sCO_2, three types of losses may occur due to condensation; kinematic relaxation losses, breaking loss, and the thermodynamic wetness loss [8], where an assessment of their impact on sCO_2 compressors is necessary. As Lettieri et al. [8] states, the thermodynamic wetness loss that takes into account the "entropy generation due to heat transfer between finite temperature differences at non-equilibrium state" is the greatest concern. This loss is estimated to take up over 45% of losses associated with phase change within steam turbines and could have a significant effect on the turbomachinery's performance. Through Starzmann and Casey's [9] study of non-equilibrium condensation effects on the performance of steam turbines, it was determined that additional thermodynamic wetness loss amounted for up to 6.5% of the total losses at one of the design conditions.

As three dimensional (3D) computational modeling is a significant tool in the design and analysis of turbomachinery, evaluation of current practices is essential to determine the accuracy when applied to sCO_2 turbomachinery. One of the main obstacles in performing computational fluid dynamics to analyze sCO_2 compressor performance and aerodynamics is the unknowns in numerical schemes ability to capture the gas dynamics of the flow around the critical point of sCO_2 due to the singular behavior of the thermodynamic properties. The desired operating conditions

for sCO_2 compressors is close to the critical point to maximize the benefits the liquid like density of the vapor within this region has on the amount of compression work required. Although this operating region displays potential pronounced benefits, the large abrupt changes in the fluid's thermodynamic properties near the critical point (Figure 4), creates difficulties when modeling within this region of interest.

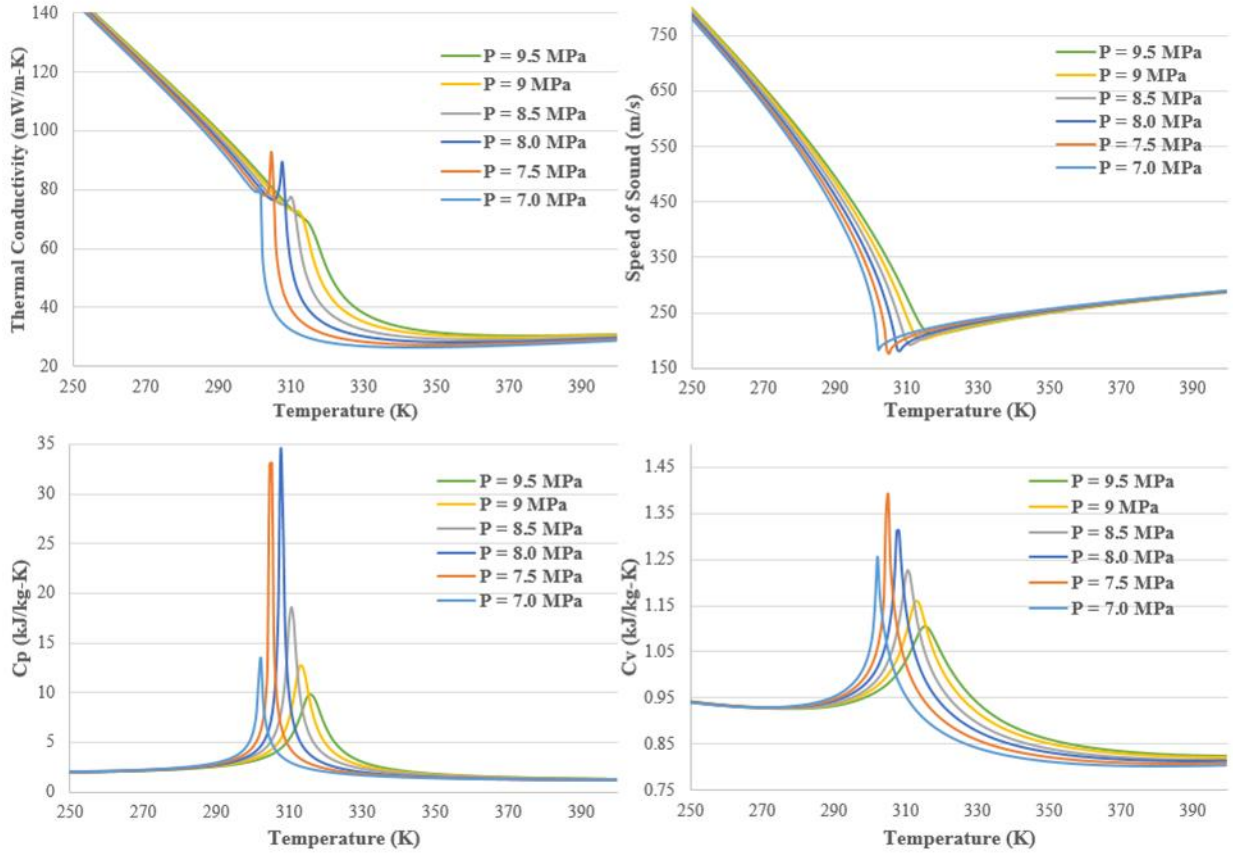

Figure 4: CO_2 Thermodynamic Property Variation vs. Temperature as a Function of Pressure

These variations cause numerical convergence issues within existing commercial design and analyses codes. As Pecnik et al. [10] and others have estimated, the local flow acceleration around the leading edge of the centrifugal impeller brings about the possibility of the static conditions entering the saturation dome. Depending on the compressor inlet conditions, this breach into the

saturation region could occur near the critical point, where variations in thermodynamic properties are heightened. These large variations in this small region increase the numerical instability within the simulation, making it necessary for one to develop a procedure, tailored to the code being utilized, to ensure convergence. Additionally, even the most accurate equation of state models cannot predict the thermodynamic properties of CO_2 in the very near proximity of the critical point. Furthermore, there is a lack of research performed within condensation phenomena for high density real gases and modeling two phase flow becomes difficult.

In order to optimize the design of sCO_2 compressors to their full potential, additional measures need to be developed in order to determine when condensation will occur and what effect it will have on the compressor performance with sCO_2 as the working fluid. If this phenomenon reduces the performance of the component greatly, criteria would need to be put into place to limit the design region to condensation free operations. High fidelity modeling techniques that can accurately predict phase change are essential to enhance the development of high efficient sCO_2 compressors. This will require a comprehensive and confirmed description of the condensation process through experimental research, entailing an assessment of the accuracy of applying the classical nucleation theory near the critical point. Further, depending on whether equilibrium or non-equilibrium phase change occurs, metastable thermodynamic properties, corresponding to a fluid state at which temperature and pressure reach values below saturation without the fluid condensating, should be implemented in modeling of the compressor. A detailed assessment of metastable thermodynamic properties of sCO_2 and when they should be applied is essential due to the lack of knowledge and research performed within metastable property definition and application space.

CHAPTER 2: LITERATURE REVIEW

2.1 Cycle Component Design and Analysis

There has been various research performed within the design and analysis of the components comprising sCO_2 Brayton cycles. While most of the research has been performed within the compressor for turbomachinery system components due to the inlet properties approaching the critical point, few studies have also been performed on designing sCO_2 turbines. Schmitt et al. [11] designed the first stage of a sCO_2 axial turbine through conventional mean line methodology and compared it to 3D computational fluid dynamics (CFD) results of the designed stage. Further, Qi et al. [12] performed a sCO_2 radial turbine design performance study as a function of turbine size parameters for the use in sCO_2 power cycles in CSP applications.

Although there are still many unknowns in the design and analysis of sCO_2 compressors, an abundance of studies has been performed in relation to this cycle component. Due to the high complexity of experimental research of these components, only a few have been carried out on the compressor. One of the well-known sCO_2 compressor test loops resides at the Sandia National Laboratory (SNL). The small scale compressor designed for sCO_2 was pioneered by Barber Nichols, Inc. with a diameter of 37 mm (Figure 5) [13].

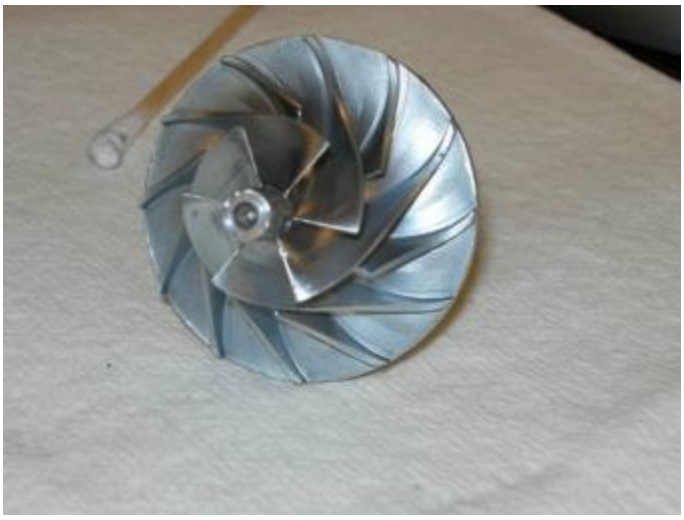

Figure 5: Main Compressor Impeller in the sCO2 Compressor Loop at SNL [13]

Wright et al. [14] presented initial test results from this loop which have been used for comparison against modeling in further computational studies. Fuller and Eisemann [13] utilized this small scale compressor test loop to evaluate off-design performance of this candid compressor. Through this it was determined that the compressor could operate over a wide range of fluid density within the supercritical region, with some inlet conditions closing in on the saturation line [13]. Brenes [15] and Vilim [16] utilized the results to compare against a 1D analysis model. Although Brenes [15] showed good agreement (peak deviation of roughly 5.5 %) to the given results, he had to estimate the dimensions of the diffuser geometry and test results through images and analysis of graphical data. Furthermore, he only could compare to the impeller exit static pressure, and the diffuser stagnation temperature and pressure, limiting the knowledge of the difference in the amount of enthalpy rise. Vilim [16] found that utilizing conventional loss models led to the necessity of adjusting the impeller loss term to bring the predicted pressure rise into agreement with SNL's testing data. He additionally notes on the limitation of understanding individual

phenomena occurring within the compressor due to selection of instrumentation points in the SNL compressor loop.

While Brenes [15] utilized total pressure loss coefficients to account for all the losses, Sanghera [17] developed a mean line code for sCO_2 centrifugal compressors in which loss models deemed optimum by Oh et al [18] were utilized to calculate all the losses through enthalpy rise in the compressor. In both Oh et al. and Sanghera's work, the loss models and the mean line code were validated against air, and hence there is a need for a further study to determine the optimal loss models for working with unconventional gases, such as sCO_2 [18], [17]. While most literature revolves around meanline design and analysis of small scale sCO_2 turbomachinery, Rahul et al. [19] [20] performed a conceptual design of turbomachinery for the use in 50 MW_e and 450 MW_e sCO_2 power cycles to replace steam Rankine Cycles for power generation from coal. Through this work, the recompressor and main compressor were sized using Balje's method and further optimized using commercial code COMPAL.

Additionally, studies have been performed within the next step of the analysis process, 3D CFD. Rinaldi et al. [21] focused on building an in-house fluid dynamic solver with a lookup table algorithm to define the fluid properties in order to develop a methodology to predict compressor performance maps. This study also utilized results from Wright et al. [14] to validate the processes. Although condensation is a possible occurrence, this phenomenon was not evaluated within this study due to the main focus being performance map matching. Rinaldi's past work with Pecnik and Colonna [22] [10] concentrated on validating numerical schemes along with the interaction between the solver and the equation of state for 3D modeling of sCO_2 centrifugal compressors working near the critical point. Through these analyses, the leading edge of the impeller blade was

established as a region where fluid properties enter the vapor-liquid region and condensation is a possible occurrence but no in depth analysis of the nucleation rate was performed.

2.2 Non-Ideal and Condensation effects of sCO_2

Further investigation into understanding the flow dynamics and flow phenomena that might occur is imperative for the optimization of the compressor within sCO_2 power cycles. The first step to accomplishing this and accurately model turbomachinery with an unconventional fluid such as sCO_2 is correctly defining the thermodynamic properties through an equation of state (EOS). Since CO_2 veers greatly from the ideal gas law along with the transpiration of large fluctuations of the thermodynamic properties within the vicinity of the fluid's critical point, this process becomes even more crucial. Due to the desired proximity of the thermodynamic properties at the inlet of the compressor to the fluids critical point, the selected EOS needs to be able to capture these large fluctuations occurring.

Two of the most widely known equation of states utilized to model the properties of CO_2 are the Span and Wagner (SW) [23] and the Lee Kesler (LK) [24] Model which were defined in 1996 and 1975 respectively. While the Lee Kesler is a commonly used EOS within the CO_2 industry, the SW model was created specifically for CO_2, whose accuracy has been shown to be around 0.05% for density [25]. Due to the model's astonishing precision, the SW model, is used by NIST to define the thermodynamic properties of CO_2 within its fluid property database, REFPROP [25]. Baltadjiev [26] performed a detailed comparison of the predicted thermodynamic properties of CO_2 from the LK model to the NIST database. Although the LK model was able to accurately determine the primary properties, such as density, enthalpy, entropy, and internal

enthalpy with an average discrepancy of 2%, the error in the derived properties was an order of the magnitude higher. This occurred due to the LK model's inability to represent the singular behavior at the fluid's critical point. In conclusion, the LK model is an accurate EOS as long as modeling is not taking place in close proximity of the critical point of CO_2. If this area is of interest, then the SW model within the NIST database is the optimum choice to define the thermodynamic properties of CO_2.

A further step into accurate modeling of cycle components with sCO_2 as the working fluid is understanding the behavior of the fluid and the flow phenomenon that might be observed that are unique to working with supercritical fluids in turbomachinery. Due to apparent diffusion process within turbomachinery, Monje et al. [27] focused on developing insight into how the parameters involved such as geometry and aerodynamics, affects the diffusion of sCO_2 flows. This was carried out through a CFD study of a conical duct where geometrical parameters, such as area ratio, and aerodynamic parameters, such as boundary layer thickness, were varied to determine the impact they had on the diffuser performance. The results from this analysis were compared to results from air diffusion experiments and it was concluded that "there exist important differences between air and sCO_2 turbomachinery that make it necessary to develop new correlations or substantial modifications of the design rules currently available in order to deploy highly efficient carbon dioxide turbomachinery" [27].

Baltadjiev et al. [28] assessed the real gas effects on the performance and matching of a candid sCO_2 centrifugal compressor through principles based modeling and further numerical simulations. Through this assessment, it was found that the compressor choke margin is reduced by 9% approaching the critical point due to the increase in isentropic exponent. Further, at high

flow coefficients, local flow acceleration around the leading edge of the impeller blade causes the thermodynamic conditions to fall below the saturation line. This conclusion exhibited the necessity for further investigation into the phase change process and accurate definitions of the fluid's metastable properties.

Lettieri et al. [8] carried out a study in which the onset of condensation is assessed through two-phase CFD analysis utilizing metastable properties of sCO_2 and a lab-scale experiment of a converging-diverging nozzle. To estimate whether condensation is an occurrence, a non-dimensional criterion was established utilizing the classical nucleation theory. This criterion relates the time required for stable liquid droplets to form to the residence time of the fluid.

To define metastable fluid properties of sCO_2 within the listed literature [8], [28] the gas properties are extrapolated onto the liquid domain. This was adopted from a similar technique utilized to create the IAPWS-97 database which defines properties for non-equilibrium condensation of water vapor in steam turbines [29]. The metastable fluid properties in this case were derived from the SW EOS using a cubic extrapolation. Utilizing this method, the spinodal line is not clearly defined but thermodynamic properties of sCO_2 never reach the spinodal limit throughout the study.

Baltadjiev [28] predicted and Lettieri [8] verified through computational analysis and experimental tests that away from the critical point the short residence time of the flow prevents condensation from taking place. Away from the critical point is defined as $S/S_{cp} > 1.01$ where S/S_{cp} represents the ratio of inlet entropy to the critical entropy. Due to the diminishing accuracy of the EOS models and the ambiguity within the accuracy of the classical nucleation theory to predict the nucleation rate in close proximity of the critical point, it is still unknown whether condensation

will occur when operating within this region. Paxson et al. [30] further validated the metastable property table methodology through blow down experiments of a converging-diverging duct. Shearing interferometer is utilized to visualize density change throughout the nozzle and the resulting measured densities are then compared to that in which are calculated through two types of metastable property tables, one developed through direct extrapolation based on the NIST SW EOS model and the other utilizing a cubic spline extrapolation from gas properties [28]. Although questions still remain on what range of conditions the extrapolation schemes for the metastable tables will hold, this study served as the first measurements of metastable sCO2 through high density shearing interferometer.

Through the various studies performed within the design and analysis of centrifugal compressors, the insufficient amount of CFD tools capable of properly determining real gas effects in the computation of thermodynamic properties has become apparent. As fully understanding the gas dynamics when working with unconventional real fluids is necessary for the accurate design of sCO_2 compressors, the past work displayed here aided in the current methodology development within computational modeling of sCO_2 turbomachinery.

CHAPTER 3: PROBLEM DEFINITION

As computational design and modeling are usually the initial step in the design process of any turbomachinery, further development of modeling tools for the analysis of sCO_2 compressors is vital for advancements and optimization of sCO_2 Brayton cycles. Currently, calculation of losses in the centrifugal compressor is an important task to achieve correct estimation of efficiency and pressure output. Since loss models developed specifically for sCO_2 have not been established yet, conventional loss models developed through experiments with ideal fluids, are used to carry out mean line analyses of these components while utilizing a real gas equation of state specific for sCO_2. The large variations in thermodynamic properties near the critical point of sCO_2 cause significant deviation from ideal gas behavior of the fluid. Additionally, the harsh operating conditions lead to a lack of experimental data in this operating vicinity, developing a need for comprehension of the applicability of conventional loss models for the success in designing turbomachinery components with this working fluid. Due to the availability of experimental data from the SNL compressor test loop, most 1D and 3D CFD analysis have been developed and validated for this specific compressor. Few in house mean line analyses have been performed on larger scale sCO_2 compressors and compared to 3D CFD [15]. Table 1 displays a comparison of past analysis performed on sCO_2 centrifugal compressors, including the cycle net power output that the compressor was designed for. Through this comparison, it is concluded that the largest cycle power output for sCO_2 compressors studied through both 1D and 3D CFD analyses was an order of magnitude smaller than the power cycle of interest within this work. As such, this work aspires to aid in the understanding of the accuracy of current mean line and 3D CFD analysis

practices and the discrepancies found between these types of analyses for sCO_2 centrifugal compressor impellers designed for large scale power cycles.

Table 1: Literature Comparison of Analyses on sCO_2 Centrifugal Compressors

	Power Specifications for Cycle Design	Mean Line (1D) or CFD (3D) analysis	P_{01} (MPa)	T_{01} (K)	s_{01}/s_{cp}	State
Baltadjiev [26]	Unkown	3D	9.35	357.15	1.33	Supercritical
			14.00	357.15	1.19	Supercritical
Bidkar et al. [19], [20]	450 MWe & 50 MWe	1D	7.70	305.15	0.95	Supercritical
			7.40	303.15	0.92	Subcooled Liquid
			7.70	305.15	0.95	Supercritical
			6.70	300.15	1.15	Superheated Vapor
Gong et al. [31]	300 MWe	1D	7.70	305.15	0.94	Supercritical
Brenes [15]	10 MWe	1D & 3D	7.50	315.15	1.22	Supercritical
			7.12	309.61	1.21	Superheated Vapor
Vilim [16] & Brenes [15]	250 kWe	1D	8.29	308.70	0.98	Supercritical
			7.92	306.78	0.97	Supercritical
			8.22	308.33	0.98	Supercritical
Ameli [32]	250 kWe	3D	7.69	306.00	1.01	Supercritical
Rinaldi [21]	250 kWe	3D	7.69	305.95	1.01	Supercritical
Pecnik [22]	250 kWe	3D	7.69	305.97	1.01	Supercritical
Rinaldi [10]	250 kWe	3D	7.69	305.95	1.01	Supercritical
Munroe [33]	Unknown	1D & 3D	9.12	308.70	0.92	Supercritical
Current	**100 MWe**	**1D & 3D**	**9.54**	**320.00**	**1.11**	**Supercritical**

For the 3D CFD analysis, in order to accurately model compressors operating with sCO_2, some modeling techniques and unique settings have to be considered. As discussed in the previous sections, there are currently difficulties in CFD modeling brought about due to the inlet to the compressor being near the critical point of this supercritical fluid. As the temperature and pressure

close in on the critical point, large variation in the thermodynamic properties of this fluid are observed. This makes it further essential to utilize a real gas equation of state (EOS) tailored to this fluid when defining its properties. Within current commercial CFD codes there are limitations to the thermodynamic property definitions available. Although some available CFD codes do have the option to utilize the NIST REFPROP database to define the fluid properties, such as ANSYS Fluent, if at any point within the solving process the fluid reaches the critical point, the simulation abruptly stops and can no longer iterate. This creates an operational boundary at which the simulation cannot be solved. Brenes et al. [15] has determined that there is a limit at which CFD with sCO_2 near its critical point can be fully carried out within the commercial solver, ANSYS Fluent. He also determined that the available cubic EOS are not able to model sCO_2 within this operating region of sCO_2 compressors, as large deviations occur in fluid properties, such as density, speed of sound and specific heat capacity. Other commercial codes do not have any available pre-defined equation of states that accurately produces the correct properties within the vicinity of the critical point for sCO_2, but do have options to create a user defined equation of state. One potential way to develop an EOS is through a user defined two dimensional temperature and pressure dependent property table, or known as a real gas property (RGP) table, to define the thermodynamic properties. The accuracy of using this option to define the equation of state was investigated within this work.

Additionally, utilizing NIST Real Gas Models (NRGM) has limitations in ANSYS Fluent, including the impossibility to model phase change or two phase flow when the NIST real gas model is utilized. This factor is also limiting the operating range in which compressors working with sCO_2 can be modeled and analyzed within the CFD code due to the potential region of

condensation at the leading edge of the blade ([22] [10] [34]). Depending on the proximity of the inlet stagnation conditions, a phase change may occur due to local flow acceleration within this area. A T-s schematic of this is displayed in Figure 6. Although, two-phase flow will not need to be simulated if the design space is constrained to condensation free regions, in order to investigate where the limits lie for this design space and how condensation will affect the performance of the compressor, modeling capabilities beyond the saturation line are needed.

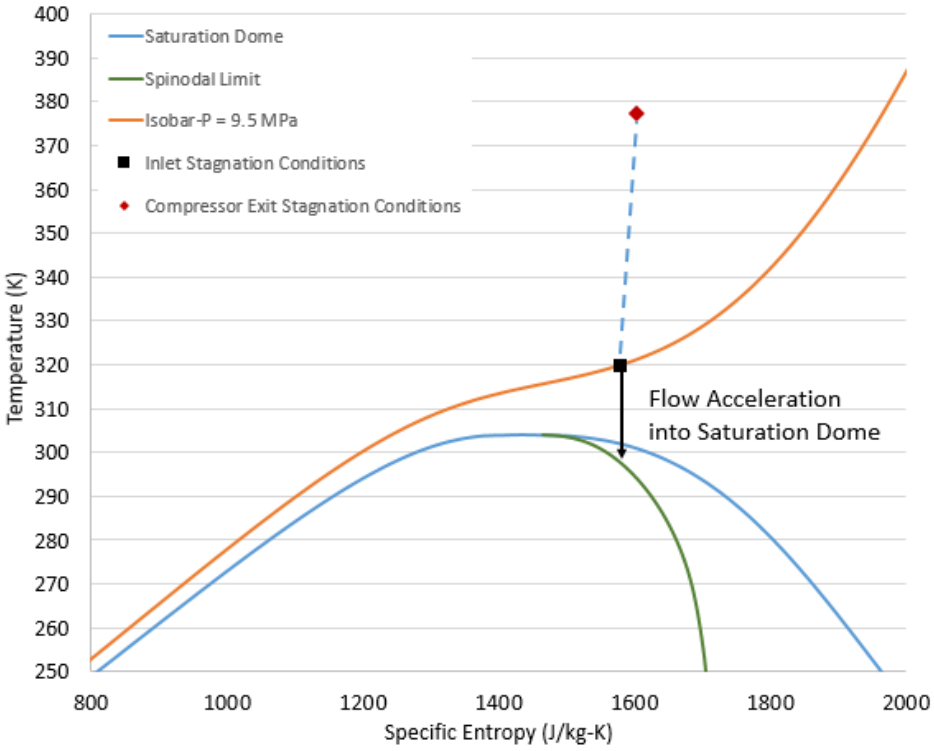

Figure 6: T-s Diagram Displaying Schematic of Local Flow Expansion

Additional aims of this work are to understand current modeling capabilities with sCO_2 as the working fluid near its critical point within the available commercial solvers. This will assist in the validation of CFD codes that can be used to aid in the design and analysis of turbomachinery operating within the supercritical state for unconventional gases. Through this, different definitions

of the thermodynamic properties will be utilized through temperature and pressure dependent tables. Metastable thermodynamic properties, which occur when a fluid reaches pressures and temperatures beneath the saturation line without condensing due to rapid expansion rates [8], are utilized to further the thermodynamic modeling range for sCO_2 compressors when performing single phase modeling. Due to the rapid expansion near the leading edge of the impeller blade, non-equilibrium condensation is predicted to occur, and thus accurate metastable properties would be needed to define the fluid within this region. Additionally, amending the equation of state with metastable properties has been considered an option to further the modeling capabilities and avoid the complication of simulating phase change and multi-phase flow. Although Paxson et al. [30] has verified these extrapolation methods through comparison of flow measurements within the metastable region for sCO_2, this was performed for a small amount of test cases that all resided away from the critical point. Due to the limited operating range that the tables were able to be tested and validated, it is still unknown under what range of conditions these extrapolation schemes are deemed accurate.

To understand how modeling sCO_2 compressors with possible two phase flow through pressure and temperature dependent property table aids in the modeling process, two types of RGP tables will be developed:

- Equilibrium Property Table generated using NIST REFPROP database, in which uses the Span and Wagner Equation of state
- Metastable Vapor Property Table generated using NIST REFPROP database that utilizes the EOS to extrapolate the gas properties into the liquid region up until the Spinodal line

The modeling capabilities and the benefits of utilizing the metastable property tables will be examined. This will be assessed through CFD analysis of a converging-diverging (CD) geometry that mimics the non-dimensional parameters of the impeller of interest. Further, an investigation of resolution of the table will be performed to determine the optimal resolution for stability and accuracy purposes while simulating flow near CO_2's critical point.

CHAPTER 4: ANALYSIS OF SCO2 CENTRIFUGAL COMPRESSORS

4.1 Methodology

4.1.1 Centrifugal Compressor under Investigation

For consistency with the CATER laboratory's previous studies on sCO_2 power cycles ([35], [36], and [11]) a closed loop Recuperated Recompression Brayton (RRC) Cycle with a net power output of 100 MW and an inlet turbine temperature (TIT) of 1350 K was the cycle specification under investigation for this study. This cycle entails a turbine, main compressor, a recompressor and a high and low temperature recuperator. The power block representation of this system can be seen in Figure 7.

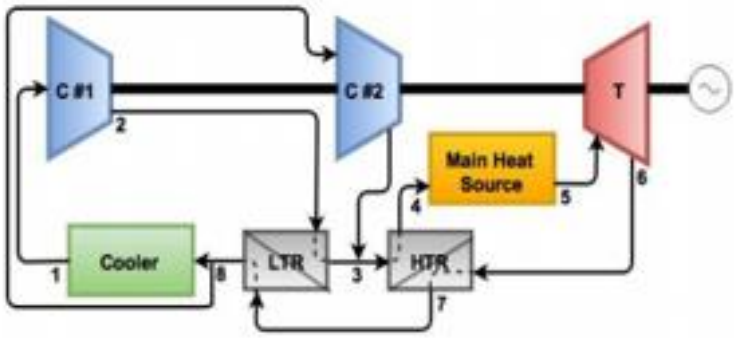

Figure 7: RRC Cycle Block Diagram

Through the methodology developed by Mohagheghi et al. [35], the thermodynamic cycle states are determined for the desired cycle TIT and power output. Table 2 displays the results of this cycle calculation.

Table 2: RRC Thermodynamic Cycle States

State Points	Temperature (K)	Pressure (kPa)	Specific Enthalpy (kJ/kg)	Density (kg/m^3)	Specific Entropy (kJ/kg-K)
1	320.0	9500	382.5	374.26	1.58
2	378.9	24000	420.5	544.16	1.60
3	487.9	23976	606.8	295.75	2.03
4	1154.4	23952	1455.6	103.75	3.13
5	1350.0	23904	1713	88.59	3.34
6	1196.6	9691	1511.8	41.91	3.36
7	498.2	9643	662.9	109.33	2.31
8	388.9	9595	529.7	162.65	2.00

The resulting T-s diagram with respect to the saturation dome of CO_2 is displayed in Figure 8. The connecting lines within the T-s diagram between the cycle state points are not exact, just schematic. One characteristic to note is the proximity of the compressor inlet condition (state 1) to the saturation dome and the critical point.

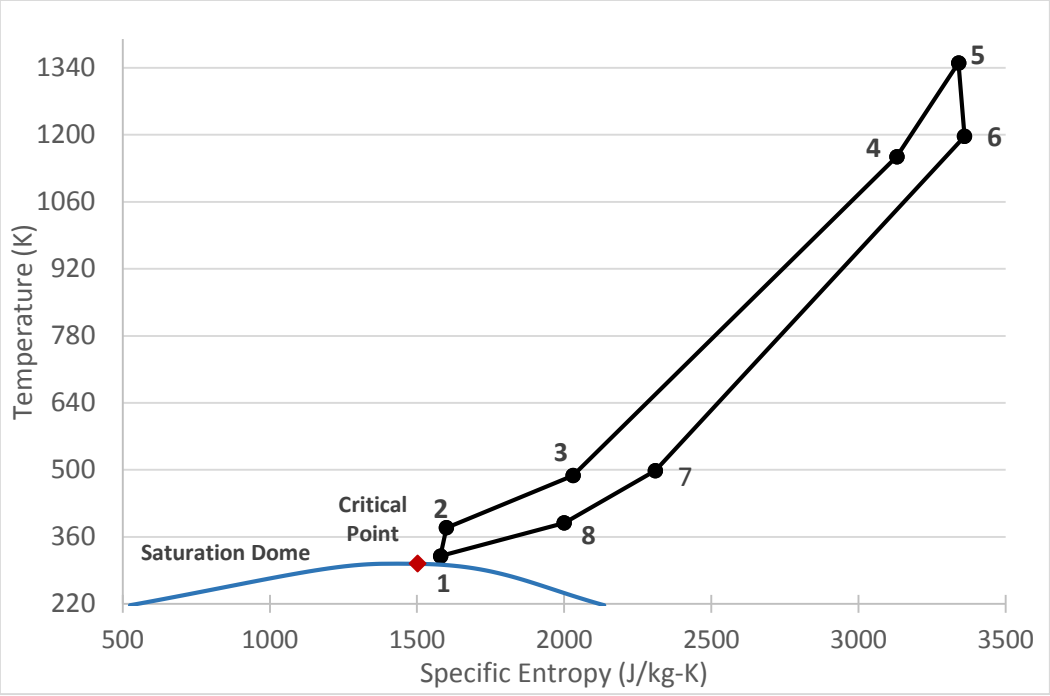

Figure 8: T-s Diagram Including Cycle State Points

Through the definition of the cycle state points, the stagnation conditions and required mass flow rate at the inlet of the compressor are determined. These parameters were used in previous work along with performance charts and specific speed and diameter, utilizing Balje's method as a starting point to design the centrifugal compressor under investigation in the current analysis presented. Only the analyses of this centrifugal compressor will be included in this work.

4.1.2 1D Analysis Methodology

4.1.2.1 Mean Line Code Development

A mean line (1D) analysis is used as the starting point for the sCO_2 centrifugal compressor analysis. The mean line analysis code utilized in this study was developed in MATLAB R2014. This uses Euler Turbine equation, Law of Conservation of Mass and Energy, and conventional centrifugal compressor loss models found in the literature to carry out the analysis. Due to large

property variations of the fluid within the operating region of the compressor, the mean line code utilizes NIST REFPROP database [25] to solve the equation of state at specified state points for CO_2. The REFPROP add-in available for MATLAB allows all included thermodynamic properties to be solved through two known thermodynamic properties. The input parameters to the code include impeller inlet stagnation properties, mass flow rate, and defined geometrical parameters. Figure 9 displays various geometrical parameters used to carry out the mean line analysis.

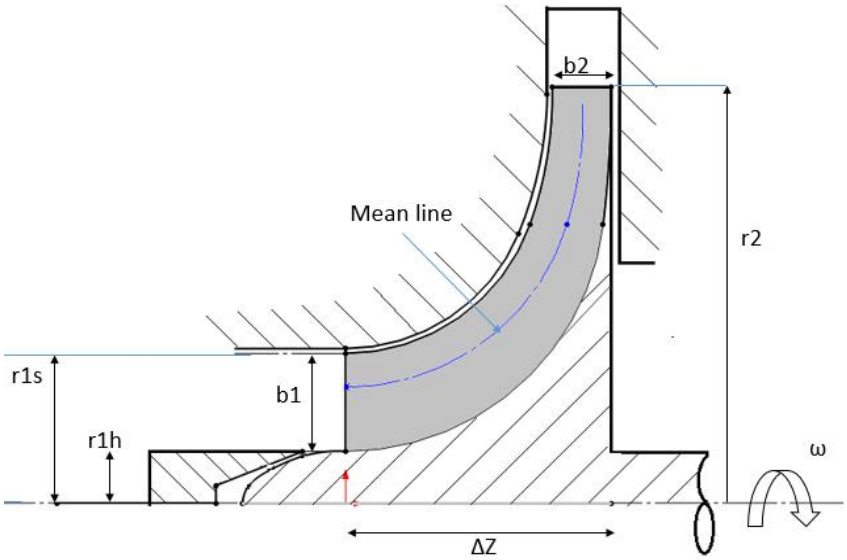

Figure 9: Schematic of the Centrifugal Compressor Impeller

The definite values for the geometrical parameters along with other input parameters for the centrifugal impeller mean line analysis are presented in Table 3.

Table 3: Definitions of the Input Parameters for the Centrifugal Impeller 1D Analysis

Main Geometrical Parameters	
Impeller Inlet Hub Radius, r_{1h}	0.1322 m
Impeller Inlet Shroud Radius, r_{1s}	0.1924 m
Impeller Exit Radius, r_2	0.2635 m
Axial Length of Impeller, ΔZ	0.144 m
Number of Blades in Impeller, Z	15
Blade Height, b_2	0.0231 m
Blade Thickness, t	0.0057 m
Cycle Specific Inputs to Mean Line code	
Inlet Total Temperature, T_{01}	320 K
Inlet Total Pressure, P_{01}	9.5 MPa
Mass flow rate, $\dot{m}$	472.2 kg/s
Input Variable	
Angular Speed, Ω	6455.3 RPM

The input variable that can be altered to obtain a desired pressure ratio is the impeller's rotational rate. Due to the selection of sCO_2 as the working fluid, and the desired inlet conditions to the compressor, further consideration has to be taken when selecting a value for this variable.

As discussed in the previous chapter, when the flow enters the compressor, the leading edge of the impeller blade causes a local flow acceleration. Depending on how close the inlet conditions to the compressor are to the critical point, this flow acceleration might cause the static conditions to fall within the saturation region of the fluid. In order to mitigate this from occurring, an isentropic expansion with the defined inlet stagnation conditions is investigated. Through the

calculation of the stagnation entropy, the equivalent saturation temperature is determined. Then using the stagnation entropy and the determined saturation temperature values, to define the state point, the speed of sound and static enthalpy are determined. A Mach number is then defined as:

$$M_{AMC} = \frac{\sqrt{2*(h01 - h(s_{01}, T_{sat}))}}{a(s_{01}, T_{sat})} \quad (1)$$

This Mach number has been termed as the Acceleration Margin to Condensation (AMC) by Brenes [15]. Due to the uncertainty in whether an equilibrium or non-equilibrium flow expansion through the vapor-pressure curve would take place, further investigation needs to be done to determine when condensation would be a physical occurrence. Although there has not been any experimental research performed on determining the onset of condensation within sCO_2 compressors, as explained in the next chapter, limitations in modeling abilities arise when approaching the critical point within the available commercial solvers. To aid in the stability within the computational fluid dynamics (CFD) analysis, assure that condensation is not an occurrence, and for comparison purposes, a safety margin between the AMC limit and the relative inlet Mach number to the impeller is put into place. The relative inlet Mach number is set to be no more than 0.8 times the determined $M_{AMC.}$ This then limits the rotational rate selected and thus the resulting pressure ratio. Through this processes, the inlet state is then fully defined.

Using the inlet velocity triangles, conservation of mass, the Euler turbine equation, and an isentropic assumption, the impeller exit conditions are initialized. Various relative total pressure losses in the compressor are then calculated using the estimated values of impeller exit velocities and thermodynamic properties. Next, an iterative process is used to reach the final converged value of total-to-total efficiency.

4.1.2.2 1D Loss Correlations

As stated in [34], the losses in centrifugal compressors can be categorized into two types; internal and parasitic losses, which cause entropy generation and total pressure loss. Internal losses originate due to non-ideal behavior of the flow, while parasitic losses arise from mechanical deficiencies in the impeller, reducing total enthalpy rise of the fluid as compared to mechanical work input by the shaft. Hence parasitic losses do not exist for stationary components of a compressor. Internal losses include sudden contraction losses, incidence losses, aerodynamic loading losses, wall friction losses, tip leakage losses and mixing losses. Parasitic losses are comprised of disk friction losses, recirculation losses, and seal leakage losses. Since the modeled impeller does not include seals or disk clearance, only the internal losses are considered in the analysis for the presented work. All impeller internal losses for the current study are calculated in terms of relative total pressure losses through a loss coefficient, ω_i and equation 2. Equation 3 then determines the relative total enthalpy at the outlet through the use of conservation of rothalpy. These two values along with the REFPROP database are used to determine the actual entropy at the outlet.

$$\boldsymbol{P_{02R} = \frac{P_{0R2,S}}{\left[1+\frac{(P_{01R}-P_1)\omega_i}{P_{01R}}\right]}} \quad (2)$$

$$\boldsymbol{h_{02R} = h_{01R} + 0.5(U_2^2 - U_1^2)} \quad (3)$$

The selected correlations for loss models were validated against results from the sCO_2 compressor loop at SNL by Brenes [15] where most have been formulated by Aungier [37]. The correlations used in this study are presented in Table 4.

Table 4: Loss Models Utilized in the Mean Line Analysis

Loss Type	Loss Correlation	
Sudden Contraction Loss	$\omega_{cont} = (r_{1h}/r_{1t})^4$	(4)
Incidence Loss	$\omega_{inc} = 0.8(1 - \frac{C_{m1}}{V_1 \cos(\beta_1)})^2 + (\frac{Zt}{2\pi r_1 \cos(\beta_1)})^2$	(5)
Wall Friction Loss	$\omega_{fr} = \frac{4C_f L_b}{D_h}(\frac{V_{mean}}{V_1})^2$	(6)
Blade Loading Loss	$\omega_{BL} = \frac{1}{24}(\frac{\Delta V}{V_1})^2$	(7)
Hub-to-Shroud Loading Loss	$\omega_{BL} = \frac{1}{6}\left[\frac{k_m b V_{mean}}{V_1}\right]^2$	(8)
Distorted Flow Loss	$\omega_\lambda = \left[\frac{(\lambda-1)C_{m2}}{V_1}\right]^2,\ \lambda = 1/(1 - B_2)$	(9)
Wake Mixing Loss	$\omega_{wake} = \left[\frac{C_{m2,wake} - C_{m2,mix}}{V_1}\right]^2$	(10)
Tip Clearance Loss	$\omega_{CL} = \frac{2\dot{m}_{CL}\Delta_{pcl}}{\dot{m}\rho_1 V_1^2}$	(11)

A sudden contraction loss takes place due to the reduction in area from the blade turning angle at the leading edge of the impeller. This is taken into account utilizing the correlation that Brenes [15] presents (eqn. 4).

Incidence losses occur when the direction of relative velocity of fluid does not match with the inlet blade angle and therefore fluid cannot enter the blade passage smoothly by gliding along the blade surface. The correlation presented by Aungier [37] is used here (eqn. 8) which takes into account the deviation of the inlet flow angle from the leading edge blade angle as well as the effect of the sudden flow area contraction due to the thickness of the blade.

Aerodynamic loading losses can be described as momentum loss due to boundary layer buildup [38] and arise from deflection of streamlines inside the impeller. This is taken into account by two loss models, one which evaluates loss occurring in the meridional direction from the

velocity distribution along the pressure and suction sides of the blades (eqn. 10) and the other evaluating the losses occurring due to the pressure gradient in the hub-to-shroud direction (eqn. 11).

Wall friction losses are calculated using a relationship given by Aungier [37] (eqn. 9) which utilizes a correlation for the coefficient of friction given by Schlichting[14] based on the average Reynolds number seen through the passage between each blade from inlet to outlet. The correlation used is specifically for turbulent flow with smooth walls and is defined as:

$$\frac{1}{\sqrt{4C_{ft}}} = -2log_{10}\left[\frac{2.51}{Re_d\sqrt{4C_{ft}}}\right] \quad (12)$$

Mixing losses account for wake mixing and flow distortion inside the impeller. Aungier [37] derived from past experimental work that distortion factor is dependent on skin friction loss for low flow coefficients, velocity head, blade aspect ratio, and the blade clearance for open impellers. Through these observations, an empirical equation for tip area blockage was formulated. This blockage factor is used to determine the amount of distorted flow losses occurring in the impeller. Mixing loss arises when the distorted flow mixes with the free stream flow. Equation 9 and 10 displays the loss models applied to determine mixing losses which involves only the meridional velocity, due to tangential velocity being restricted by the conservation of angular momentum.

The centrifugal compressor is being modeled as an open impeller and thus relative total pressure losses occur due to the clearance gap leakage and the difference in pressure from the suction to the pressure side of the blades. The relationship presented in Aungier [37] (eqn. 11) is

used in this study where the average pressure difference across the gap and the amount of blade clearance gap leakage flow are estimated from eqn. 3 and 4 respectively.

$$\Delta \boldsymbol{P_{cl}} = \frac{\dot{\boldsymbol{m}}(\boldsymbol{r_2 C_{\theta 2} - r_1 C_{\theta 1}})}{\boldsymbol{Z \bar{r} \bar{b} L}} \quad (13)$$

$$\boldsymbol{m_{cl}} = \boldsymbol{\rho_2 Z \delta_{TCL} L V_{CL}} \quad (14)$$

The calculated internal loss coefficients described here are then used in eqn. 1 to calculate the relative total pressure. Using the resulting value for this and the relative total enthalpy at the outlet, the actual entropy is then determined, $s_2 = s(h_{02R}, P_{02R})$.

The slip factor occurs when the flow is not entirely guided by the blade angle at the exit and there is deviation of the flow angle from the blade exit angle. This is calculated based on work by Wiesner [39] with correction implemented by Aungier [37].

$$I_B = \sigma \left(1 - \frac{\lambda \dot{m} \tan(\beta_2}{\rho_2 A_2 U_2}\right) - \frac{U_1 C_{\theta 1}}{U_2^2} \quad (15)$$

$$\Delta h_0 = I_B U_2^2 \quad (16)$$

In order to calculate the actual change in enthalpy, the blade work input coefficient correlation presented by Aungier [37] is utilized (eqn. 15 and 16). Through this calculation the total-to-total isentropic efficiency can be calculated. Furthermore, the absolute total pressure can be found using the actual entropy and enthalpy at the exit and the REFPROP database, $P_{02} = P(h_{02}, s_2)$. The actual pressure ratio is then determined. The h-s diagram schematic for this mean line analysis method is displayed in Fig. 3.

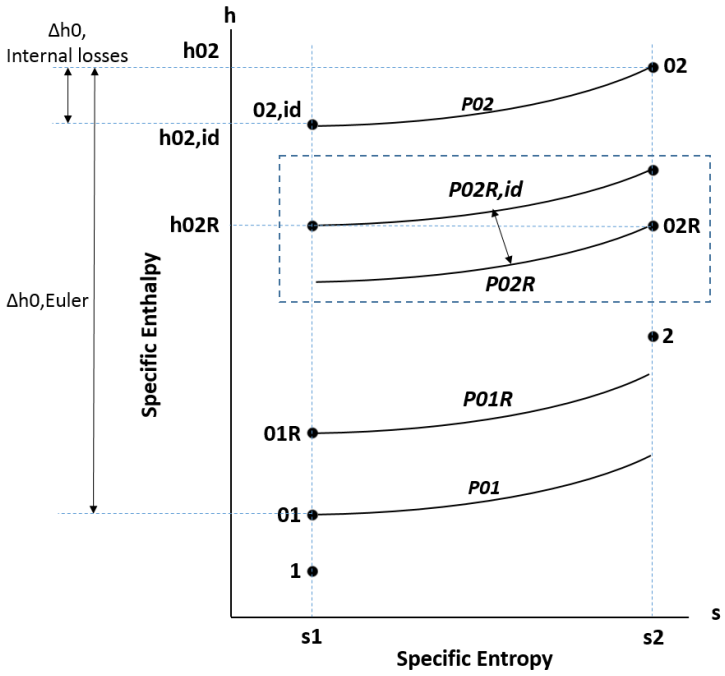

Figure 10: h-s Diagram Schematic including Isobars for Centrifugal Impeller State Points

Due to a vaneless diffuser included in the CAD model of the impeller utilized in the 3D analysis, outlet conditions of the vaneless diffuser have to be solved for in order to have an estimate of the outlet boundary conditions. Through the known increase in radius from the impeller outlet to the diffuser outlet the ideal static pressure rise can be determined using conservation of angular momentum and conservation of mass. Further, a diffuser loss factor, κ_d, for the vanless diffuser is implemented through the correlation:

$$\boldsymbol{P_{03} = P_{02} - \kappa_d(P_{02} - P_2)} \quad (17)$$

This takes into account compressibility effects. Typical values of κ_d vary from 0.01 to 0.4 [17]. The diffuser loss factor, κ_d is iterated here through the comparison to the calculated κ_d value obtained through the CFD results.

4.1.2.3 Validation of 1D Centrifugal Compressor Analysis Code

In order to validate the accuracy of the mean line analysis code developed, the geometry and test results from the SNL sCO_2 compressor experimental test loop were utilized. Due to the limited experimental measurement locations within this test loop and vaned diffusers not being examined in the 1D analysis code, only a comparison can be made for the impeller outlet static pressure. Three different test results were utilized to compare where the geometrical parameters and the experimental results were taken from Vilim [16]. The input parameters along with the deviation from the experimental results can be seen in Table 5. The code results displayed an average deviation of 5.12% for the static pressure where the 1D code overestimates this value. Given the instrumental uncertainty provided by Vilim [16], the mean deviation can be reduced. Although this deviation is higher than desired, given that this is a 1D analysis, utilizing conventional correlations with an unconventional fluid, this deviation is deemed satisfactory to utilize in the comparison against the 3D analysis prediction.

Table 5: Comparison of 1D Analysis Code Results to Experimental Results from the SNL sCO2 Compressor Experimental Loop

	Test 1	Test 2	Test 2	Instrumental Uncertainty (±)
P_{01}	8.286	8.224	7.920	0.02 MPa
T_{01}	308.700	308.333	306.778	0.2 C
RPM, Ω (krpm)	64.380	59.584	29.888	N/A
MFR	2.860	2.609	1.315	0.05%
P_2 (Experiment)	10.670	10.260	8.264	0.02 MPa
P_2 (Mean Line Code)	11.323	10.816	8.579	
Deviation from Experiment (%)	6.120	5.419	3.812	

4.1.3 3D CFD Analysis Methodology

4.1.3.1 Geometry Definition

The commercial solver, ANSYS Fluent was utilized to carry out the presented steady state CFD study. As to mitigate the mesh size and simplify the solving process and to obtain accurate periodic interfaces of the 15 blade centrifugal compressor impeller, a 24 degree section with a single blade is modeled. The impeller model was created in SolidWorks and can be seen in Figure 11.

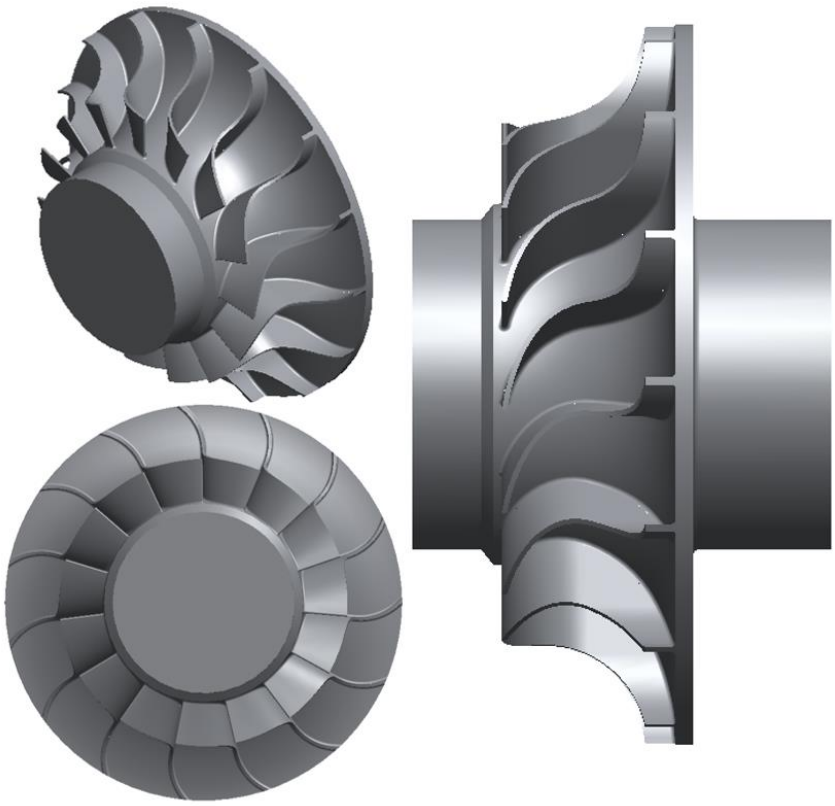

Figure 11: (Clockwise from Top left) Impeller-Iso, Impeller-Right, and Impeller-Front

The 24 degree section of the compressor channel can be seen in Figure 12. The 3D model includes the clearance gap between the impeller tip and the shroud as well as a vaneless space after

the impeller exit plane. This is modeled to aid in numerical stability and mitigate negative flow going back into the compressor channel.

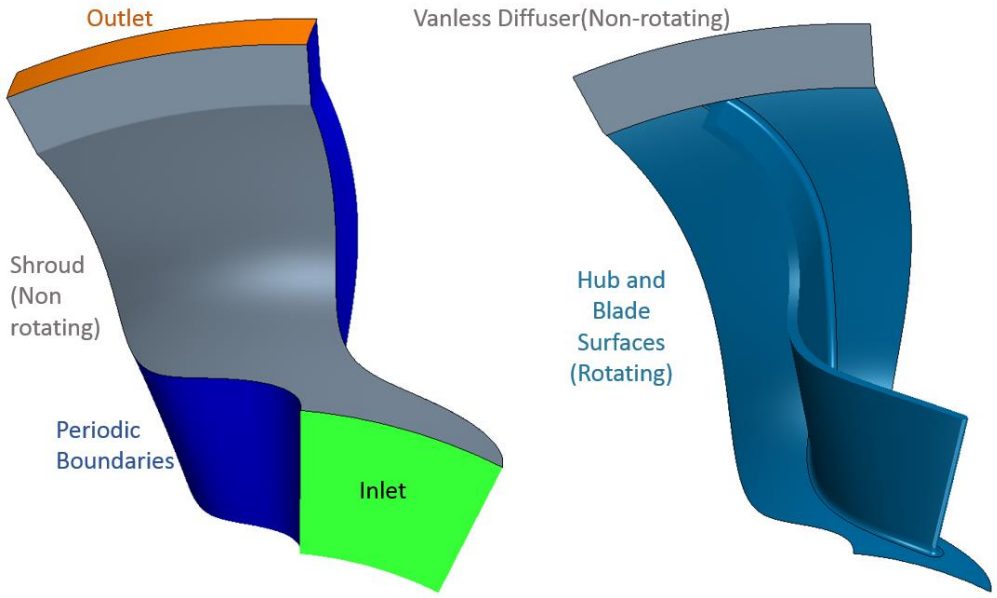

Figure 12: 24 degree Centrifugal Impeller Geometry Definition

4.1.3.2 Solver Settings, Boundary Conditions, and Near Wall Treatment

A mesh was generated with a combination of unstructured polyhedral and prism layer cells. As near wall treatment depends on the turbulence model used, two options for turbulence modeling were considered. The first option that is very popular within modeling turbomachinery and has been used within modeling sCO_2 turbomachinery specifically in the past ([22] [10]), is the Shear-Stress-Transport (SST) version of the k-ω turbulence model. Although utilizing this model improves the wall treatment, the requirement of a mesh refinement near the wall creates a very computational costly simulation. Another exceptionally plausible option is the Realizable k-Epsilon model, which has also been utilized in sCO_2 compressor modeling [33], [15]. This option, coupled with implementing wall functions, is an acceptable alternative when a coarser mesh is

needed due to computational constraints. As there were limitations to the amount of computational power available, the latter option has been chosen to carry out this study. All wall y+ values lie within the suggested range when using the standard wall function, available when k-epsilon turbulence models are used, in which y*~y+ should lie within the range of 30 < y* <300 [40]. Figure 13 displays the mesh including near wall grid refinement at the mid-span around the leading edge and the trailing edge of the blade.

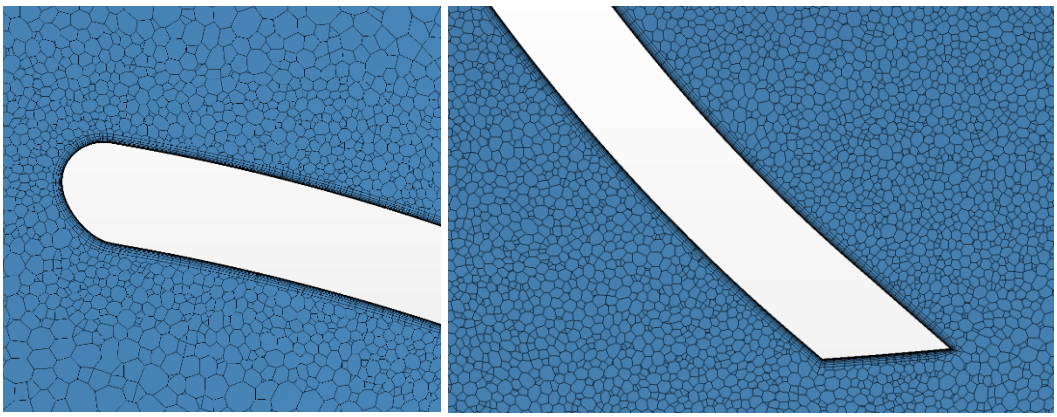

Figure 13: Mesh at Mid-Span around the Leading Edge and the Trailing Edge of the Impeller Blade for the Finest Mesh

The pressure based coupled solver was utilized to solve the compressible Reynolds-Averaged Navier-Stokes equations (RANS) in Fluent. In order to aid in convergence, a courant number equal to 1 was set along with first order upwind interpolation schemes. Thermodynamic properties of real gas sCO_2 were modeled using a two dimensional thermodynamic property table, dependent on temperature and pressure. This was created with the use of the NIST real gas model, REFPROP database [26] that is a real gas model embedded into Fluent. Utilizing the option to generate tables within Fluent does not allow you to specify the resolutions of the tables. As this has been determined in the later chapters to affect the accuracy of the real gas model, this method is not the most ideal method to define sCO_2 properties. One can call to the REFPROP database

directly within Fluent but this slows down the solving process immensely. For this reason, the embedded real gas property table is used and the discrepancy between the interpolated values to the results from the REFPROP database are determined.

The impeller blade rotation was modeled using the moving reference frame method to obtain a steady state calculation. For this method, a relative reference frame is created with the specified rotational rate while all wall boundaries are set to moving rather than stationary. Depending on whether the surface is a rotating wall or not, zero velocity is applied with respect to either the relative or absolute reference frame. For this, the hub and blade surfaces are set to zero velocity with respect to the relative reference frame while the shroud and vaneless diffuser surfaces have zero velocity with respect to the absolute frame. All wall boundaries are set to smooth and adiabatic, with a no slip condition.

The inlet and outlet boundaries of the model were set to a mass flow inlet and pressure outlet respectively, with total temperature prescribed at the inlet and backflow total temperature at the outlet. Boundary parameters were set according to the parameters calculated through the mean line analysis. For the inlet and outlet surfaces, turbulence viscosity ratio and intensity were set to 10% and 5% respectively for both boundaries.

When utilizing the REFPROP database for the equation of state, caution has to be taken as to not fall into the saturation dome or the simulation will be halted due to two phase flow occurrence. As such, to aid in limiting this occurrence and to assist in numerical stability, lower limits of temperature and pressure within the domain are set slightly away from the critical point of CO_2. These limits were set to 305 K and 7.5 MPa for temperature and pressure respectively

during the initial solving process. Due to these limitations, meeting lower limit of temperature and pressure warnings occurred and decreased throughout the solving process.

Convergence was determined through monitoring mass imbalance along with inlet static and total pressure and outlet total pressure. As the mass imbalance approached a value of the order of a thousandths decimal place and the pressure monitors were steadying off to one value, the lower limit for pressure was slowly decreased to 6.0 MPa while the lower limit for temperature was decreased to 304.5 K. Lowering these limits removed the limiting pressure warnings and reduced the amount of limiting temperature warnings, although few cells still met the temperature limit even after the simulation was deemed converged.

4.1.3.3 Grid Convergence Study

To estimate the discretization error within the mesh size, a mesh independence study was performed where three meshes were studied. The sizes of these meshes can be seen in Table 2.

Table 6: List of Mesh Sizes Investigated

Mesh Number	Total Number of Cells
3	4711377
2	7040669
1	9916809

The result comparison for the impeller inlet and outlet variables can be seen in Table 7. To quantify the discretization error, the grid convergence index (GCI) methodology presented by Celik et al. [41] was utilized to calculate the GCI along with extrapolated values and the estimated extrapolated approximate error from the finest mesh for temperature, pressure, and absolute and relative velocity. These properties were utilized due to the equation of state being define by

temperature and pressure along with the stagnation properties dependency on the velocity. The resulting values for the approximate relative error,e_a for the three meshes studied and the grid convergence index, GCI_{fine}^{21}, are also displayed in Table 2. Due to limitation in computational power and the results for the finest mesh showing a relative error to the extrapolated value below 1% for every variable besides the absolute velocity at the inlet, this mesh has been chosen to carry out the rest of this study.

Table 7: Grid Convergence Results

	Mesh 3	Mesh 2	Mesh 1	e_a^{32}(%)	e_a^{21}(%)	GCI_{fine}^{21}	Extrapolated Value	e_{ext}^{21}(%)
$\bar{P}_{01}$	9.631	9.566	9.532	0.686	0.354	0.752	9.475	-0.605
$\bar{T}_{01}$	319.651	319.900	319.957	0.078	0.018	0.010	319.983	0.008
$\bar{P}_1$	9.544	9.481	9.450	0.668	0.333	0.654	9.400	-0.526
$\bar{T}_1$	319.197	319.491	319.546	0.092	0.017	0.007	319.565	0.006
$\bar{C}_1$	19.475	20.246	20.564	3.808	1.542	2.042	20.899	1.607
$\bar{V}_1$	112.691	112.834	112.858	0.126	0.022	0.009	112.866	0.007
$\bar{P}_{02}$	18.776	18.533	18.590	1.309	0.307	0.150	18.612	0.120
$\bar{T}_{02}$	361.646	361.033	361.001	0.170	0.009	0.001	360.998	-0.001
$\bar{P}_2$	13.620	13.451	13.472	1.251	0.156	0.038	13.476	-0.031
$\bar{T}_2$	342.929	342.001	341.945	0.271	0.016	0.002	341.939	-0.002
$\bar{C}_3$	143.305	144.414	144.641	0.768	0.157	0.075	144.728	0.060
$\bar{V}_3$	73.628	68.649	69.182	7.252	0.770	0.162	69.271	0.129

Further look into how the mesh resolution affected the flow field inside the compressor was performed through generating circumferential absolute velocity and static pressure profiles at the Mid-span for the impeller outlet and the diffuser outlet (Figure 14). This displayed significant deviation in profiles from the coarsest mesh (Mesh 3) to the finest (Mesh 1). Although still visible,

less differences were observed between Mesh 1 and Mesh 2. This suggests that further look into local GCI is beneficial when property profiles are of concern rather than averaged values.

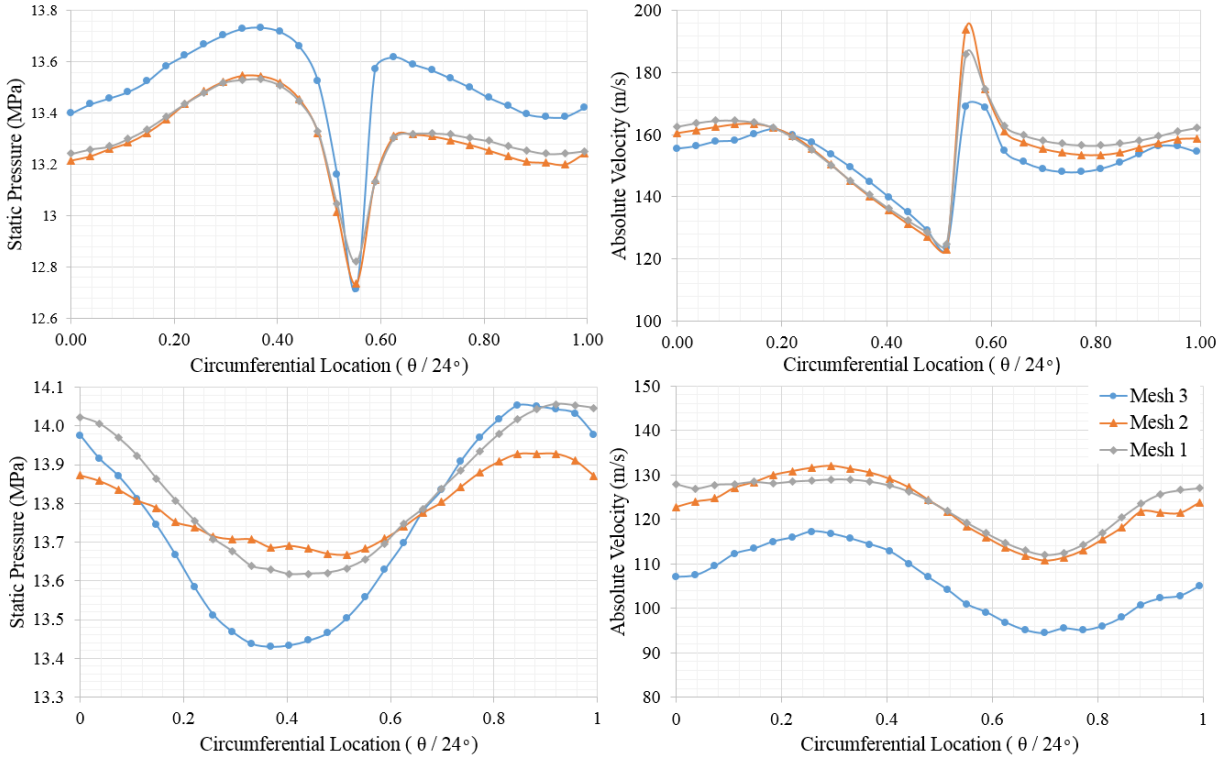

Figure 14: Circumferential Absolute Velocity and Pressure Profiles at Mid-span for Impeller Outlet (Top) and Diffuser Outlet (Bottom) for the Three Meshes

Additionally, the average static and total pressure at the mid-span of the blade along the stream-wise direction were compared for the three meshes (Figure 15). This displayed less dependency on mesh resolution for the resulting pressure gradients along the stream-wise of the blade due to better agreeance between the profiles for the three meshes.

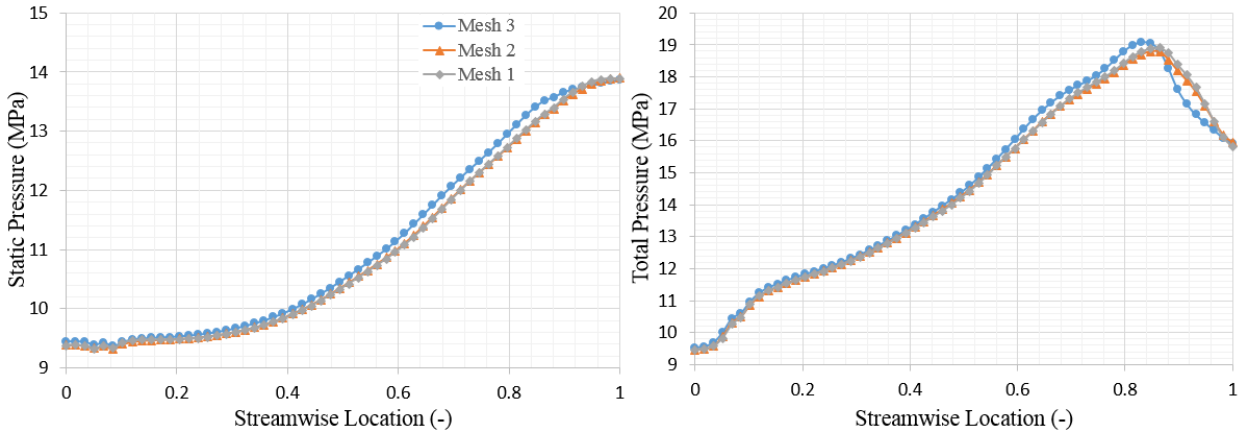

Figure 15: Comparison of Mid-span Static Pressure (Left) and Total Pressure (Right) Along the Stream-wise Direction of the Blade Passage for the Investigated Meshes

Through the numerical uncertainty analysis, Mesh 1 was deemed satisfactory to carry out this study. For future performance analysis for off-design operation comparison, further investigation within numerical uncertainty for capturing local flow dynamics will be performed.

4.2 Analyses Results

4.2.1 1D Analysis Results

The mean line analysis yields thermodynamic properties along with absolute and relative velocity components at the inlet and outlet of the compressor impeller. The resulting static and stagnation temperature and pressure along with the absolute and relative velocity magnitude at these locations are displayed in Table 8. The resulting stagnation pressure is less than the desired main compressor output stagnation pressure of 24 MPa, displayed in Table 2, suggesting that multiple compressor stages may be needed for the compression process.

Table 8: 1D Analysis Resulting Property States for Impeller Inlet and Outlet

Property	Impeller Inlet	Impeller Outlet
P0 (MPa)	9.532	16.729
T0 (K)	319.957	355.083
P0R (MPa)	11.962	14.206
T0R (K)	333.525	345.134
P (MPa)	9.454	13.066
T (K)	319.462	340.026
ρ (kg/m3)	377.771	432.882
C (m/s)	20.361	126.404
V (m/s)	111.588	71.862
β'	79.487	-35.218

Figure 16 displays the contribution of each type of loss in the compressor impeller for the resulting relative stagnation pressure loss coefficients. These are calculated using loss correlations that were previously discussed in the 1D Analysis Methodology section. Incidence, sudden contraction, and wake mixing losses take up most of the losses occurring within the impeller, where as wall friction losses barely account for a quarter percent (0.29%) of the resulting losses.

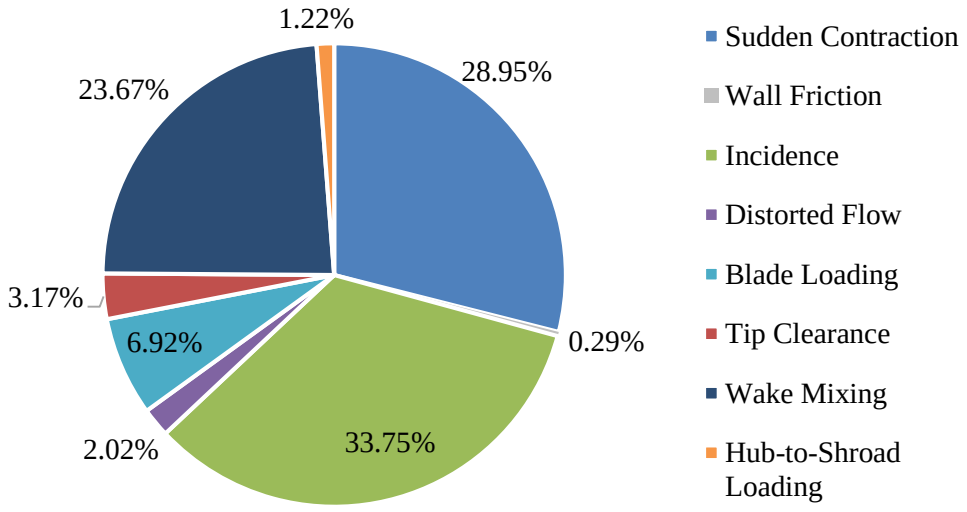

Figure 16: Distribution of the Losses Calculated through Mean Line Analysis

The estimated total-to-total isentropic efficiency for the compressor impeller obtained through this analysis was 76.77%. This is a lower value observed when compared to past sCO_2 compressor impeller analysis [15]. Additionally, the relative flow angle at the impeller exit is around -35˚ compared to the -45˚blade angle at the trailing edge. This suggests that the flow is not fully guided by the blade and slip is occurring.

4.2.2 3D CFD Analysis Results

The CFD analysis allows for prediction of inlet and outlet property state points while also providing insight into the flow field within the domain. The resulting mass average static conditions along with the absolute and relative velocity at the impeller inlet and outlet are displayed in Table 9. With these values known, all other properties of the fluid can be determined.

Table 9: Resulting Impeller Inlet and Outlet State from CFD Analysis

	Impeller Inlet	Impeller Exit
$\bar{P}$ (MPa)	9.450	13.574
$\bar{T}$ (K)	319.546	341.945
$\bar{C}$ (m/s)	20.564	144.641
$\bar{V}$ (m/s)	112.858	69.182

To inspect the accuracy of utilizing the embedded NIST real gas model through temperature and pressure dependent property tables, mass average reports for each property are compared to exact values derived from the NIST REFPROP database. All of the static properties are found using the mass average reports of temperature and pressure within ANSYS Fluent and the REFPROP database, which only needs two properties to define the state. Then the total properties are found using the known correlations for absolute and relative stagnation enthalpy:

$$h0 = h + 0.5C^2 \quad (18)$$

$$h0R = h + 0.5V^2 \quad (19)$$

Due to the entropy remaining the same for static and stagnation properties, the static entropy along with the stagnation enthalpies calculated through equation 18 and 19 were used in the REFPROP Database to determine the stagnation properties. Through this process, the accuracy of using the option to create a temperature and pressure dependent property table to decrease the computational time was assessed. The mass averaged reports from Fluent and the derived REFPROP properties along with the deviation of the two for each property are displayed in Table 10. The deviation from the properties calculated through REFPROP for the impeller exit state are all less than 1% besides the relative stagnation pressure, an exceptional deviation for the time saved by using this option. The impeller showed much larger deviations with one of the more significant concerns being the 4% deviation in density, a property that greatly effects the velocity. Higher deviations are observed in the secondary properties such as dynamic viscosity, thermal conductivity, and isobaric specific heat. The higher deviations found at the impeller inlet could be a result of the static properties relatively closer distance to the critical point. The proximity of the fluid properties to the critical point was found to have an impact on the resulting interpolation error in the next chapter of this work.

Table 10: Predicted State Properties for the Impeller Inlet and Exit through Mass Average Reports and utilizing REFPROP Database

	Impeller Inlet			Impeller Exit		
	Mass Ave Report from CFD	Calculated from REFPROP	% Deviation from REFPROP	Mass Ave Report from CFD	Calculated from REFPROP	% Deviation from REFPROP
P0 (MPa)	9.532	9.529	0.029	18.692	18.561	0.702
T0 (K)	319.957	320.051	-0.029	361.001	360.795	0.057
P0R (MPa)	12.125	12.005	1.006	14.832	14.656	1.201
T0R (K)	333.447	333.915	-0.140	347.180	346.581	0.173
h0 (kJ/kg)	377.553	381.692	-1.084	404.276	404.408	-0.033
h0R (kJ/kg)	384.720	387.849	-0.807	396.003	396.340	-0.085
s (kJ/kg-K)	1.563	1.576	-0.820	1.582	1.583	-0.072
h (kJ/kg)	378.351	381.481	-0.820	393.610	393.947	-0.086
ρ (kg/m3)	390.460	375.594	3.958	445.835	444.425	0.317
Cp (kJ/kg-K)	6.806	6.713	1.378	3.556	3.553	0.074
k (kW/m-K)	54.383	53.568	1.521	52.642	52.524	0.225
μ (kg/μm-s)	28.984	27.678	4.721	33.309	33.145	0.496
a (m/s)	215.086	211.475	1.707	258.176	257.791	0.150

The option to utilize a temperature and pressure dependent table derived from REFPROP rather than the solver calling to the REFPROP database at every iteration for each state is a considerable option to save computational time. The drawback to this option is the uncertainty and inability to control the resolution of the table. This could create substantial extrapolation error when solving for properties even closer to the critical point, where larger variations are observed and have significant effects on the solution obtained.

To further look into the flow through the impeller, the absolute and relative velocity vectors at the mid-span of the blade are displayed in Figure 17. The relative velocity exhibits significant

recirculation occurring from the suction side of the blade while the flow seems to be well guided by the blade nearing the pressure side of the blade.

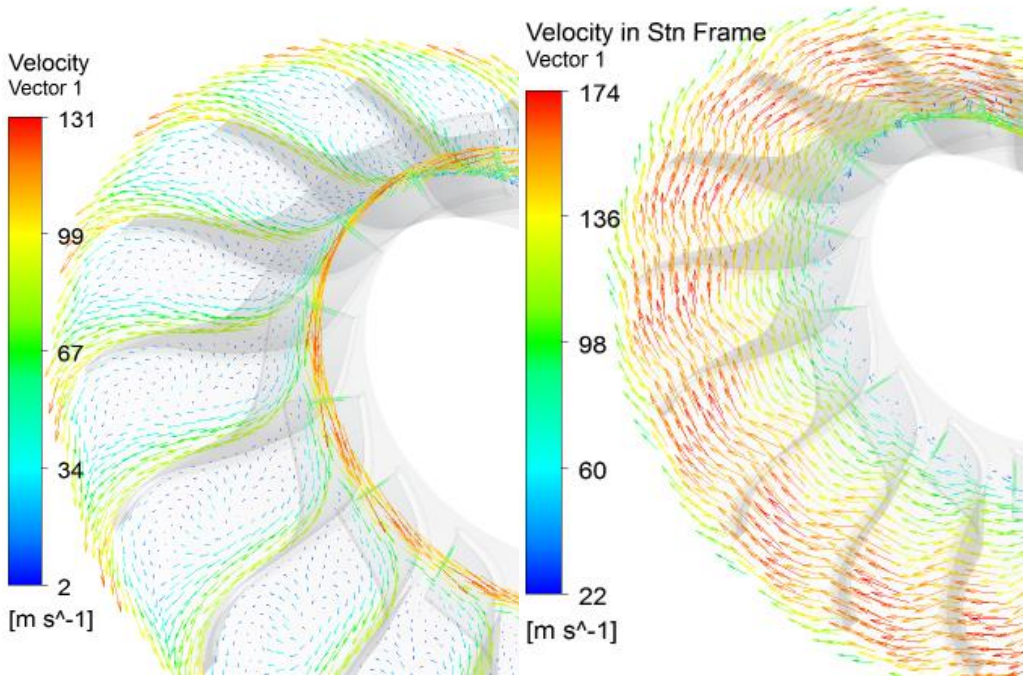

Figure 17: Relative (Left) and Absolute (Right) Velocity Vectors at Mid-Span of the Impeller

Static pressure contours along the blade and the hub surfaces of the impeller as well as the blade-to-blade plane at the mid-span of the blade are displayed in Figure 18, where small areas are seen at the leading edge of the impeller blade in which pressure falls below the critical pressure of 7.3773 MPa.

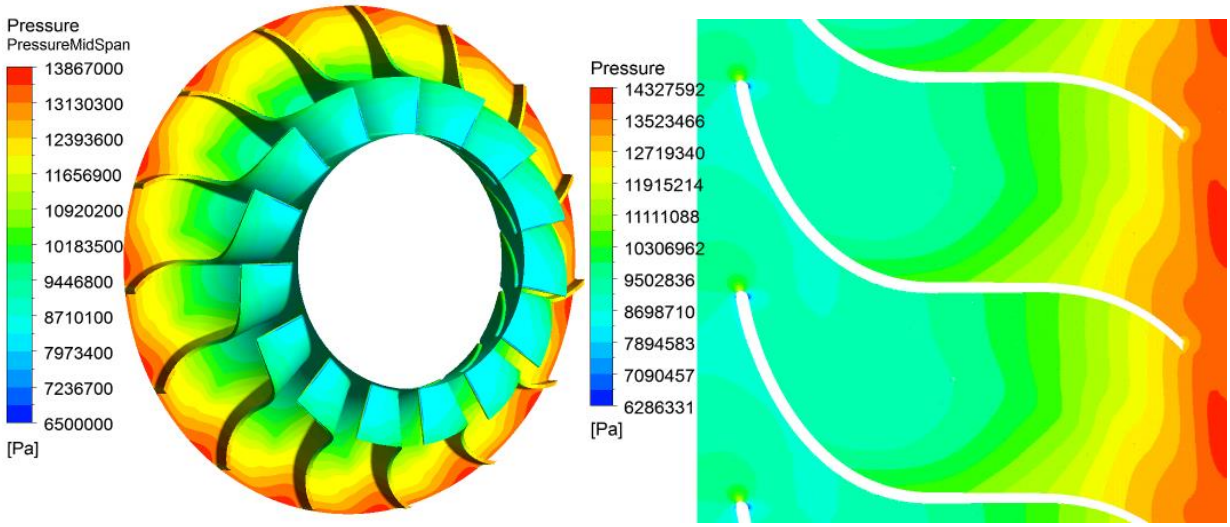

Figure 18: Static Pressure Contours along the Blade and Hub Surfaces (Left) and in the Blade-to-Blade Plane at Mid-Span (Right)

To investigate this region further, cells which have pressure values less than or equal to the critical pressure along with a temperature that meets the minimum temperature of 304.5 K are determined. This resulted in very few cells located at the leading edge of the blade. The area that met this criterion can be seen in Figure 19 in which are highlighted green.

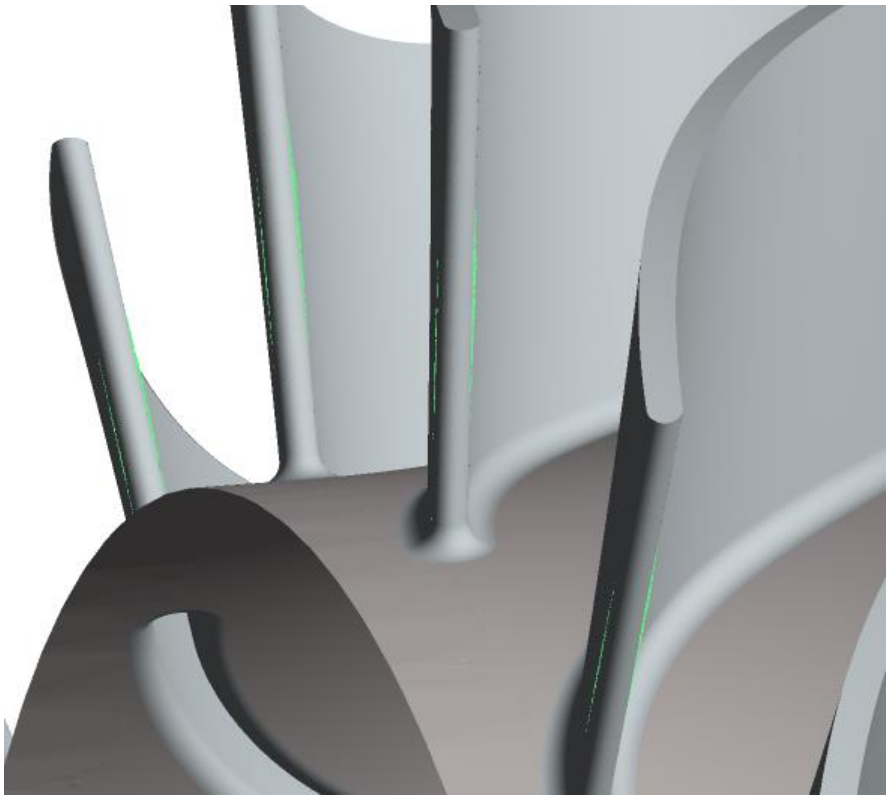

Figure 19: Iso-Volume Highlighting in Green the Locations in Which Meet or Fall Below the Critical Pressure and Meet the Set Minimum Temperature within the Impeller Domain

Due to the inability to model close to the critical point and to model two-phase flow in Fluent, from this observation no conclusion can be made as to whether temperature and pressure values would surpass the saturation line. Since there was only a small amount of area which meet this criteria, condensation was not a concern within the operating conditions set for this compressor and using the AMC limit was deemed successful.

4.2.3 1D and 3D Analyses Comparison

To understand the discrepancies between the two analysis methodologies and determine the differences that lie within the results obtained, Table 11 displays the values obtained for the main parameters of interest through the two analyses and the deviation of the 3D results from the 1D analysis. While the inlet conditions match relatively well between the 1D and 3D analyses,

with the largest deviation seen in density being attributed to the interpolation error within this property, the impeller outlet results show significant differences between the two analyses. The largest thermodynamic property difference is seen in the stagnation and static pressure, where these values obtained through the 3D analysis are significantly higher than that of the 1D result. One observation that this can be attributed to is the resulting large deviation seen in the magnitude of the absolute and relative velocity between the two analyses.

Table 11: 3D Analysis Deviation from 1D Results

	Impeller Inlet			Impeller Outlet		
	1D	3D	Deviation from 1D (%)	1D	3D	Deviation from 1D (%)
P0 (MPa)	9.532	9.532	0.000	16.729	18.692	11.731
T0 (K)	319.957	319.957	0.000	355.083	361.001	1.667
P0R (MPa)	11.962	1.454	0.444	14.206	14.336	0.914
T0R (K)	333.525	-0.037	0.103	345.134	347.180	0.593
P (MPa)	9.454	9.450	-0.042	13.066	13.574	3.885
T (K)	319.462	319.546	0.026	340.026	341.945	0.564
ρ (kg/m3)	377.771	390.460	3.359	432.882	445.835	2.992
C (m/s)	20.361	20.564	0.997	126.404	144.641	14.428
V (m/s)	111.588	112.858	1.138	71.862	69.182	-3.730
beta	79.487	79.604	0.147	-35.218	-42.214	19.863

For further investigation into the comparison of the two analyses, some main performance parameters, such as the total relative pressure loss coefficient, total-to-total impeller efficiency, slip factor, and the area blockage factor at the impeller exit were calculated for the 3D analysis. The total relative pressure loss coefficient was calculated using equation 2, where the ideal relative stagnation pressure at the impeller exit, $P_{02R,S}$ was calculated using the mass average results for entropy at the inlet and the resulting relative stagnation enthalpy at the exit, $\bar{P}_{02R,S} = P(\bar{s}_1, \bar{h}_{02R})$.

The total-to-total isentropic efficiency was calculated in a similar way, where the ideal stagnation enthalpy at the exit was defined as $\bar{h}_{02,S} = h(\bar{s}_1, \bar{P}_{02})$ and equation 20 was used to calculate the total-to-total efficiency.

$$\eta_{tt,1-2} = \frac{\bar{h}_{02,S} - \bar{h}_{01}}{\bar{h}_{02} - \bar{h}_{01}} \quad (20)$$

The area blockage factor, B_2 was calculated using equation 21 where the mass average report values at the impeller exit were used for the absolute meridional velocity at the exit and the normal area was calculated in Fluent.

$$\dot{m} = \bar{\rho}_2 \bar{C}_{m2} A_2 (1 - B_2) \quad (21)$$

The slip factor was determined through the evaluation of the ideal tangential velocity compared to the resulting tangential velocity in the absolute reference frame. To calculate this, the meridional velocity was assumed constant between the ideal and real velocity triangles and the blade angle at the exit was used as the relative flow angle for the ideal velocity triangle.

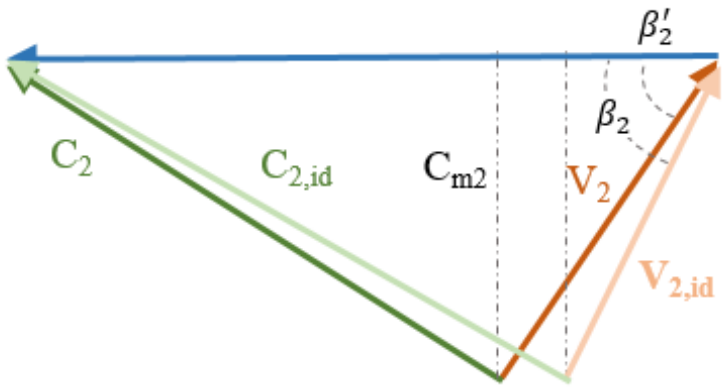

Figure 20: Ideal and Real Impeller Exit Velocity Triangle Example

Figure 20 displays the ideal versus the real velocity triangles at the exit of the impeller blade where the magnitude of vectors and angles are not exact, just schematic. Through the calculation of these

parameters, the two analyses methods were further compared. The prediction of these parameters for both analyses can be seen in Table 12.

Table 12: Comparison of Aerodynamic and Performance Parameters between the Analyses

	3D (Derived from Mass Ave Reports)	1D
Total Loss Coefficients, ω	0.963	0.772
Efficiency, $\eta_{tt,1-2}$	74.113	76.710
Impeller Exit Flow Angle, β_2' (deg)	-42.214	-35.218
Slip Factor, σ	0.988	0.874
Blockage Factor, B2	0.400	0.253

Through the comparison of the results from the two analyses carried out, a few observed differences to note are:

- The sum of the loss coefficients was 20% smaller in the 1D analysis than in the 3D even though the 1D results in a lower relative and absolute stagnation pressure at the exit of the impeller. This result can be contributed to the 0.82 % interpolation error found in inlet entropy and further the 1.2% error in the relative stagnation pressure at the impeller exit. These deviations skew the resulting relative stagnation pressure to be higher for the 3D analysis although there are more losses predicted to occur.
- The predicted efficiency in the 3D analysis was 3.4% lower than that of the 1D analysis. As blockage factor has a large impact on the blade work input coefficient and thus the total enthalpy rise (eqn. 16), the higher blockage factor in the 3D analysis may take some of the responsibility for the lower efficiency observed as well.

- There was less slip observed in the 3D analysis, where the relative flow angle at the trailing edge of the blade was guided more by the blade angle than what was determined in the 1D analysis

Furthermore, the 3D analysis resulted in a total pressure ratio of 1.96 compared to the value of 1.76 obtained through the 1D analysis. Due to the limitation of the rotational rate through the inability to model two-phase flow, neither of the analyses meet the desired pressure ratio for the compressor of 2.53.

4.3 Chapter Summary

The current study presents comparison of 1D analysis with 3D CFD analysis of a centrifugal compressor impeller with sCO_2 as the working fluid. Since compressor seals and disk clearance are not modeled in the present work, the main focus of the mean line method is analysis of internal losses and their effects on efficiency and total pressure ratio. Additional look into other performance parameters led to a more in-depth comparison of the two analyses. A 100 MW closed loop sCO_2 RRC Brayton Cycle mean line analysis yields impeller inlet conditions along with desired outlet conditions. Initialization of iterative process for loss calculations is done using isentropic impeller exit conditions, later losses are used to calculate efficiency and other performance parameters of the impeller. Additionally, a safety margin from the AMC Mach number with respect to the relative Mach number at the impeller inlet is put into place as a precaution to condensation occurrence. This is also utilized to aid in numerical stability within the 3D analysis by preventing the fluid from entering into the two phase region within the compressor channel. Outputs of the mean-line analysis are used as boundary conditions for the CFD case.

The CFD analysis of the open impeller is carried out in ANSYS Fluent which utilizes a two dimensional property table created in REFPROP that is embedded in the code and uses a bi-linear interpolation method to obtain the thermodynamic properties of sCO_2. When comparison of the interpolated property values to the exact values calculated using the REFPROP database, significant deviation from the REFPROP derived values were observed, especially for density, dynamic viscosity, and isobaric heat capacity for the inlet boundary location. The average deviation from the REFPROP value for all the properties listed at the inlet was 1.38%. On the contrary, the average deviation from the REFPROP values for the properties at the impeller exit was 0.28%, a value that should not be detrimental to the solution obtained. The large deviations observed at the inlet are believed to be due to the relatively close proximity of the static conditions to the critical point.

An aerodynamic analysis is performed through the resulting CFD study. The CFD also provides an opportunity to visualize the flow field within the impeller and further inquire into how effective the impeller blade angles and streamlines are at turning the flow. As such, very little insight into these phenomena are given through a mean line analysis. When comparing the two predicted resulting analysis for the specified centrifugal impeller, a few significant differences are observed.

CHAPTER 5: INVESTIGATION OF SCO2 PROPERTY MODELING THROUGH CFD OF A CONVERGING-DIVERGING DUCT

Through the 3D analysis of the centrifugal impeller with sCO_2 as the working fluid, further understanding of the modeling difficulties and limitations that are brought about when working with sCO_2 near the fluid's critical point are developed. Within the chosen CFD commercial code, ANSYS Fluent, it is not possible to model two phase flow of CO_2 and further utilizing the embedded REFPROP tables to define the equation of state for CO_2 limits the modeling region to above the saturation line. For this reason, the defined modeling process is limited to the predicted condensation free regions, determined by utilizing a safety factor from the AMC limit, discussed in more detail in Chapter 4. Another drawback to using this method to simulate sCO_2 turbomachinery is the inability to control the table resolution and thus the interpolation error when using the NIST real gas property table option within ANSYS Fluent. To further the modeling region of the centrifugal compressor without adding the complexity of simulating two phase flow, utilizing metastable property tables is a proposed methodology. Metastable thermodynamic properties arise when non-equilibrium condensation occurs.

As explained in Lettieri et al. [8], due to the rapid expansion rate, the fluid can reach pressures and temperatures below saturation without condensation. This is illustrated schematically in Figure 21 [26]. Whether condensation occurs due to this breach into the saturation region depends on the nucleation rate versus the residence time that the fluid stays at this state. Baltadjiev applied the classical nucleation theory to sCO_2 compressor flows which led to the conclusion that because of large nucleation time and the relative small residence time within the

saturation region, condensation would not be an occurrence for states away from the critical point [28]. This work is not focused on the investigation of nucleation rates but rather the accuracy of using the RGP tables to represent the equation of state and how embedding these tables with metastable properties furthers the capable thermodynamic modeling region.

Although this work is not targeted towards understanding sCO_2 flow leaks through seals, the same principles can be applied to further understand leakage flow through labyrinth seals.

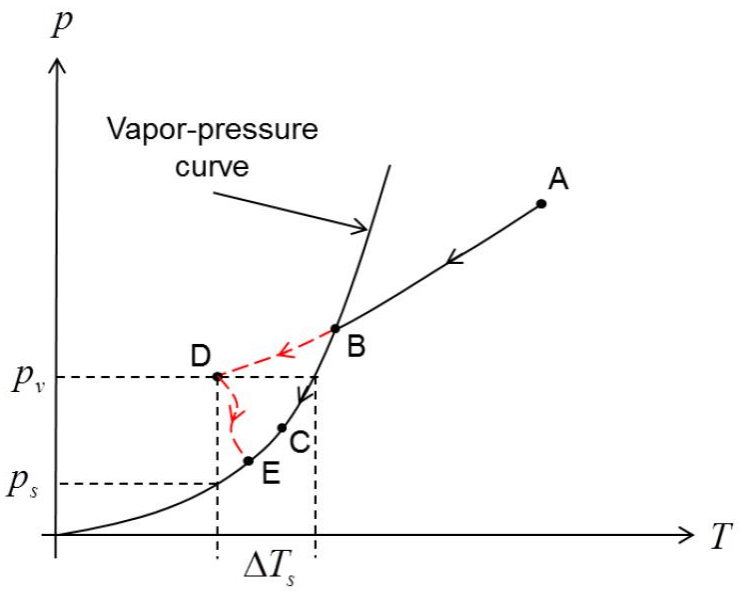

Figure 21: Equilibrium (ABC) and Non-Equilibrium (ADE) Flow Acceleration through the Vapor-Pressure Curve [26]

5.1 Methodology

5.1.1 3-D Modeling Methodology

As the flow through a converging-diverging (CD) duct can be utilized as a simplified representation of the flow dynamics around the leading edge of the compressor blade and the diffusion processes thereafter, this type of geometry is chosen to carry out this study.

Table 13: Various Geometric Parameters to define CD Nozzle

Geometry Definition	
D_{th} (mm)	5
A_{exit}/A_{th}	2.7
A_{in}/A_{th}	4
L_{div}/D_{th}	11.02
L_{conv}/D_{th}	0.543

The 3D model of the CD duct along with the surfaces of interest are displayed in Figure 22. This model was made to be geometrically similar to the impeller blade passages, having the same area ratio and length to diameter ratio from inlet to outlet as the compressor.

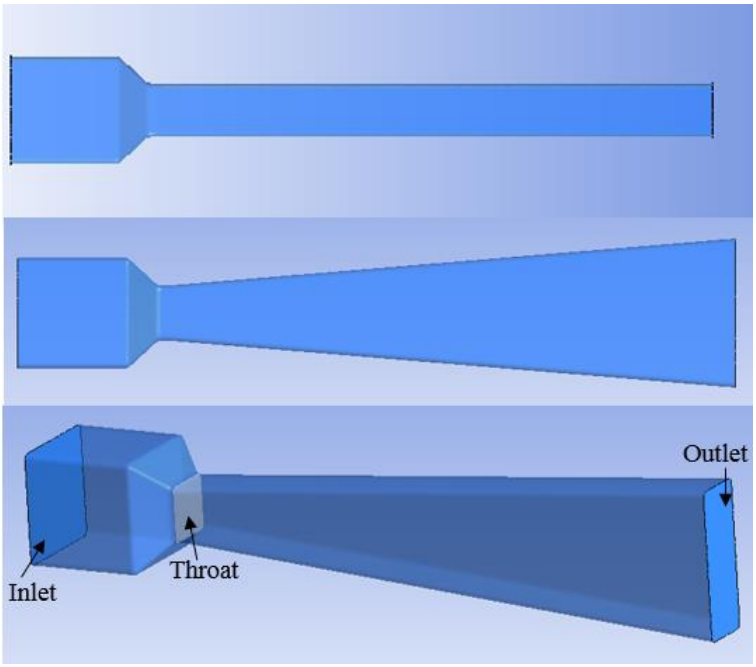

Figure 22: CD Nozzle Top, Side, and Isometric Views (from Top to Bottom)

The CFD study of the converging-diverging duct is carried out in the commercial solver, ANSYS CFX in which utilizes a fully coupled solver. This solver is chosen due to the ability to create user defined real gas property tables dependent on temperature and pressure to define the

fluid thermodynamic properties. The turbulence model selection was kept the same as stated in Chapter 4, with k-ε Realizable model as the turbulence model specified with a scalable wall function implemented. All wall y+ values were within the suggested range when using the scalable wall function, in which y*~y+ should lie within the range of $30 < y^* < 300$ [40]. The unstructured mesh was created with a mixture of tetrahedral and prism layer cells with a total of 3.2 million cells. In order to get estimation of the mass flow rate through the duct along with the pressure at the outlet to use as boundary conditions, a 1D iterative calculation of the diffuser was performed, where the inlet stagnation properties were chosen in terms of their proximity to the critical point and outlet conditions were calculated through assumption of an isentropic processes. Static pressure rise coefficient for the diffusion process was estimated from Brenes' work on 2D diffusers with sCO_2 as the working fluid [15]. To set the mass flow rate, the Mach number was chosen dependent on the desired position of the static properties in relation to the saturation line. Utilizing REFPROP's option to solve vapor phase only, metastable properties can be used to estimate the amount the static properties will exceed the fluid's saturation line. Total properties were used as initial conditions for speed of sound and density and then further recalculated with static enthalpy through the initialization of velocity with the set Mach number. Once converged to a set of total and stagnation properties at the throat of the CD duct, the mass flow rate, area ratio of the entrance to the CD Duct and throat, along with the inlet total properties were used to estimate the inlet boundary conditions while the estimated static pressure was used at the outlet boundary condition.

Once the boundary conditions were established, the simulation was performed with the established RGP table to define the equation of state, which will be further explained in the next section of this chapter. In order to reach convergence, small time steps were required along with a

blending factor for the advection scheme of 0.25, where 0 is equivalent to first order and 1 is second order. Convergence criteria for all residuals was set to below 0.0001 while stagnation and static pressure at the inlet and the stagnation pressure at the outlet were all monitored to ensure these parameters had less than a 0.1% change. Additionally mass imbalance was monitored throughout the iterative process to ensure that there was no mass imbalance occurring through the domain.

5.1.2 Thermodynamic Properties Table Definition

Through the option for the user to create a real gas property (RGP) table dependent on temperature and pressure within ANSYS CFX, it is possible to personalize the property range that will be solved for along with the value for the required property at the corresponding temperature and pressure. The RGP table option requires the user to provide values for entropy, enthalpy, specific volume, speed of sound, dynamic viscosity, thermal conductivity, isobaric specific heat capacity (Cp), isochoric specific heat capacity (Cv), and the partial derivative of pressure with respect to specific volume at constant temperature, $\left(\frac{\partial P}{\partial v}\right)_T$ at every combination of T and P. In order to define where the phase stops, an accurate representation of the phase change line for the liquid has to be included. For equilibrium phase change, this line would be the saturation line of the fluid but considering the concern within the occurrence of non-equilibrium phase change, the spinodal limit was specified as the limit of the vapor phase. The differences in these two lines can be seen in Figure 23 along with the differing equilibrium and non-equilibrium values for enthalpy and speed of sound in terms of temperature and pressure. As stated in the previous sections, an established way to define metastable properties is through extrapolation of gas properties into the liquid region. Although the range at which utilizing this technique to represent the metastable fluid

properties is accurate for has yet to be determined, a comparable method has been used in the past to simulate non-equilibrium condensation in steam turbines [28]. To define the metastable properties within this work, REFPROP's definition of metastable properties through the direct calculation from the Span and Wagner equation of state within the liquid region without taking into account the fluid's two phase nature at this state is utilized [42]. This method is executed up until the spinodal limit, at which further breach into the saturation region would result in condensation and thus liquid properties are specified thereafter. To visualize the resulting differences between equilibrium and non-equilibrium fluid properties as they are defined here, enthalpy and speed of sound surface contours in terms of temperature and pressure are displayed in Figure 23. The saturation line and the spinodal line are displayed in the non-equilibrium plots to show where the extrapolation of the gas properties starts and ends.

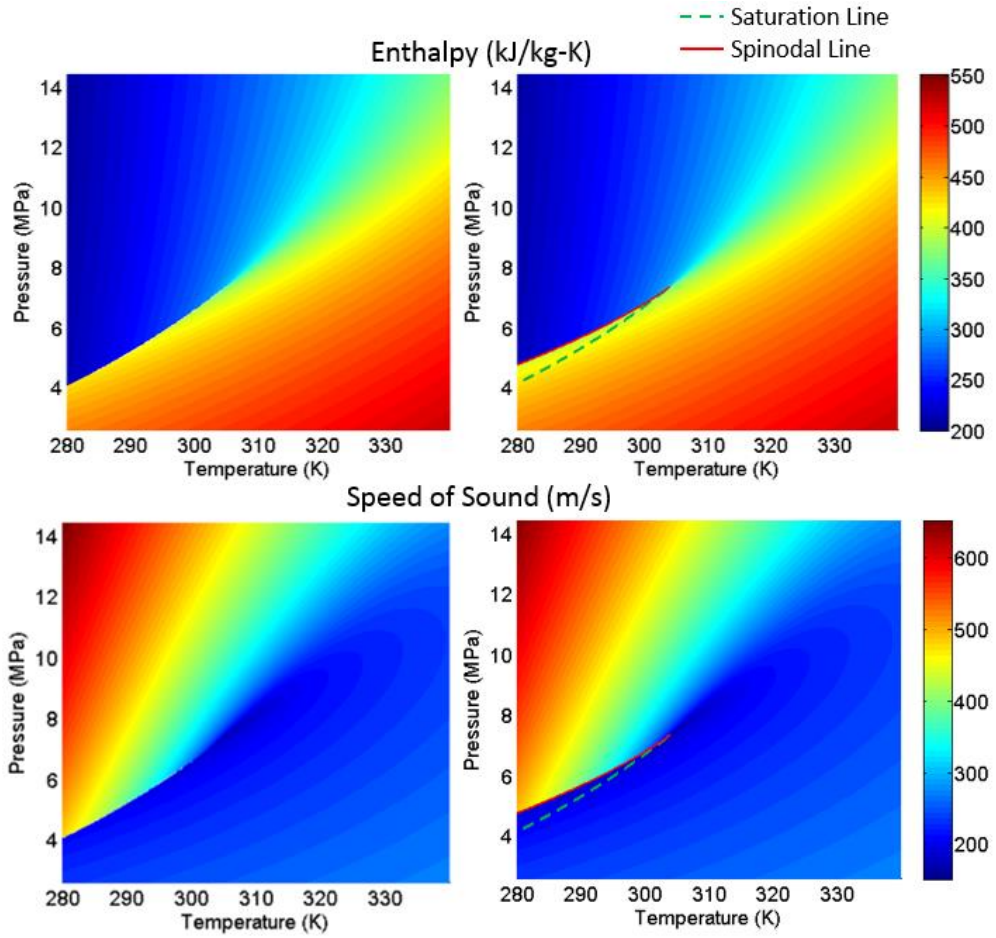

Figure 23: Surface Contour of Equilibrium (Left) and Non-Equilibrium (Right) Enthalpy (Top) and Speed of Sound (Bottom) in terms of Pressure and Temperature

In order to determine how the resolution of the RGP table affects the accuracy of the result obtained, a study was performed in which the interpolated error was investigated. This was performed through evaluating the deviation of the mass average values obtained from the CFD solution to the exact calculated value from REFPROP with various RGP table resolution for temperature and pressure. The three tables that were used to carry out this study are present in Table 14, with Table 1 being the coarsest and Table 3, the finest.

Table 14: Resolution Definition for the Three RGP Tables Utilized

	Size	Temperature Range and Resolution (K)	Pressure Range and Resolution (MPa)
Table 1	100 x 100	280 : 0.5 : 329.5	2.5 : 0.25 : 27.25
Table 2	150 x 150	380 : 0.3 : 324.7	2.5 : 0.10 : 17.40
Table 3	600 x 600	280 : 0.1 : 339.9	2.5 : 0.02 : 14.48

Three sets of boundary conditions were utilized to perform this study with various proximity to the critical point. Two sets of boundary conditions modeled static conditions at the throat of the CD duct that were approaching, but keeping some distance from the saturation dome. The third set of boundary conditions was fixed so that the flow properties would reach the saturation dome at the throat. To visualize the flow expansion process occurring, each case is plotted against a T-s diagram that includes the saturation dome and vapor spinodal limit (Figure 24). The cases are represented by the stagnation properties and the respective static properties at the CD throat, making up the line representing the flow acceleration.

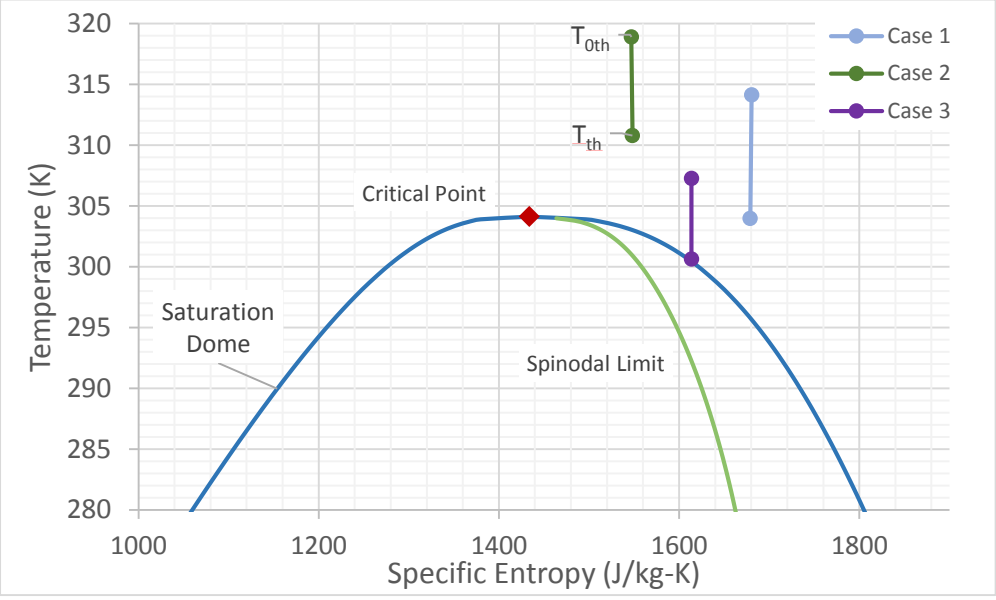

Figure 24: Visualization of Flow Accelerations through the Nozzle Throat on a T-s Diagram

The cases were defined through the ratio of stagnation pressure, stagnation temperature, and entropy to their respective critical value (Table 15). The interpolation error with respect to the ratios defined was compared to determine if the proximity of the fluid properties to the critical point has an effect of the accuracy obtained. Case 1 and 2 were utilized to first understand the accuracy of the tables when only modeling above the saturation line to limit the complexity of the simulation. Then Case 3 was carried out to further investigate the error obtained between two tables with different resolution when fluid properties reach the saturation line. Additionally, Case 3 was carried out to determine how utilizing the metastable properties through the RGP table aids in expanding the capable modeling operating range within single phase calculations.

Table 15: Definition of the Stagnation Properties Selected for the Three Flow Accelerations Modeled

	Case 1	Case 2	Case 3
$P_{0,th} / P_{cp}$	1.075	1.295	1.040
$T_{0,th} / T_{cp}$	1.033	1.049	1.009
s_{th} / s_{cp}	1.171	1.080	1.113
M_{th}	0.474	0.440	0.400

5.2 CFD Results

For Case 1 and 2, modeling with RGP Tables 1 and 3 were carried out to investigate the interpolation error associated with defining the EOS through temperature and pressure dependent tables and thus the desired Mach number at the throat was kept constant for the two cases. Properties that show large fluctuations when approaching the critical point and were thought to have the most effect on the solution, such as density, specific heat, and entropy were chosen for comparison. To obtain the exact value for the property from the REFPROP database, the mass

flow average of the static pressure and temperature at each boundary were utilized to solve the equation of state. The property values for each location of interest (inlet, throat, and exit) were taken from the solution through mass flow average reports. The percent deviation is said to be the interpolation error and was defined for each property, ϕ, as:

$$e_{int} = \frac{\phi_{CFD} - \phi_{NIST}}{\phi_{NIST}} X\ 100 \quad (22)$$

A comparison of the resulting interpolation error when using Table 1 and 3 are presented for Case 1 and 2 in Table 16. The largest error occurred at the throat of the CD nozzle for each property and for every case the property with the greatest amount of interpolation error was Cp. Through the observation of the highest error occurring at the throat, it can be said that the proximity to the saturation dome has a significant effect on the resolution of the table needed to get satisfactory low interpolation error. Further investigation into the comparison of the two tables shows that for both cases, Table 3 seems to be sufficient enough to capture all the fluctuations occurring where the only error larger than 1% is seen in Cp. Results obtained when using Table 1 indicate larger deviation from the exact calculation of this property, with a 6.25% deviation observed in Cp for Case 2. Due to the inability of Table 1 to represent the fluid properties, this table will be discarded for the remainder of this study. Some differences in the errors obtained within each property are seen between Case 1 and Case 2, where when using Table 3 Case 1 displays greater interpolation error overall. When investigating the differences in the property ratios for these cases displayed in Table 15, the temperature and pressure ratios are closer to the critical point for Case 1 while the entropy ratio is closer to the critical value for Case 2. This suggests that there is more impact on the error received from the location of the fluid entropy to the critical point rather than the other properties investigated

Table 16: Deviation of Mass Average Property Values from REFPROP Calculated Properties for Case 1 and 2

Case 1	Property	CD Inlet	Throat	CD Exit
Table 1	Density	0.221	0.343	0.110
	Entropy	-0.050	-0.160	-0.030
	Enthalpy	-0.036	-0.045	-0.003
	Cp	1.244	3.290	0.803
Table 3	Density	-2.153E-04	-0.247	-4.94E-04
	Entropy	1.457E-04	0.034	-6.45E-05
	Enthalpy	2.977E-04	0.071	3.55E-04
	Cp	0.001	-1.067	4.67E-04
Case 2	Property	CD Inlet	Throat	CD Exit
Table 1	Density	0.416	0.681	0.167
	Entropy	-0.089	-0.011	-0.036
	Enthalpy	-0.121	-0.048	-0.034
	Cp	0.141	6.250	-0.266
Table 3	Density	0.293	-0.777	0.099
	Entropy	-0.065	0.194	-0.021
	Enthalpy	-0.118	0.243	-0.028
	Cp	0.526	2.192	0.250

To further investigate how the interpolation error affects the solution obtained, the resulting Mach contour at the mid-plane of the nozzle when utilizing the two different tables was compared for Case 1 and 2 (Figure 25). For Case 1, no real visual differences is observed between the two contours when modeling with Table 1 or Table 3. When examining the same contours for Case 2 however, visual differences can be seen between the images from utilizing the coarsest table to the finest table. When looking at the interpolation error of the resulting speed of sound, Table 1 and Table 3 produces an error of 0.6% and 0.24% respectively for this case. Although the resulting error does not seem significant, even the 0.4% decrease in deviation from the exact value can have a visual impact on the flow field obtained within modeling. This further supports the suggestion

that the non-linear behavior of the fluid can be captured further through more resolved RGP tables and that the resolution of the tables has more impact when entropy is closing in on the property's critical value.

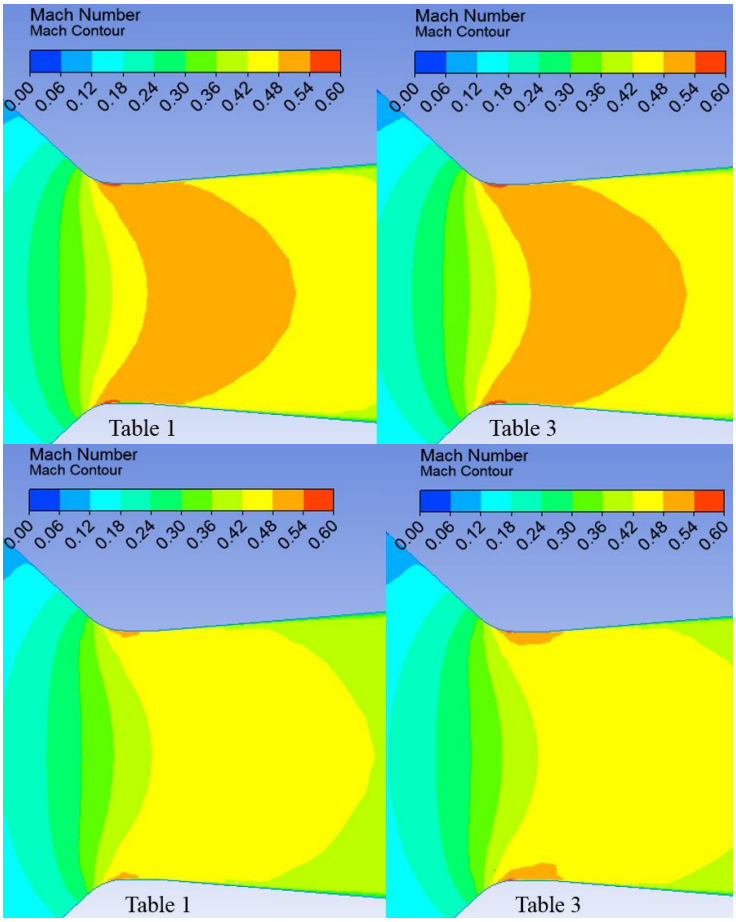

Figure 25: Mach Profiles through the CD Nozzle Mid-Plane using Table 1 (Left) and Table 2 (Right) for Case 1 (Top) and Case 2 (Bottom)

Further scrutinization of the interpolation error obtained from using a RGP table was performed for Case 3, where properties surpass the saturation line at the throat of the CD nozzle. This was modeled using Table 2 and 3. When evaluating the interpolation error obtained with Table 2, a 17% and 1.7% deviation from the exact value for Cp and density was observed respectively at the throat. Further, significant deviations occurred for Cp at the inlet and outlet

surfaces as well. Although Table 2 is the medium resolution table, this case resulted in a higher deviation for Cp and density than what was determined for Case 1 and 2 when the coarsest table was implemented. Density resulted in a 1.64% deviation, being 8 times the amount of error observed when Table 3 was used as the thermodynamic model. On the contrary, the resulting table comparison for Case 1 and Case 2 exhibits the error in density staying relatively the same.

Figure 26: Deviation of Mass Average Property Values from REFPROP Calculated Properties for Case 3

Case 3	Property, ϕ	CD Inlet	Throat	CD Exit
Table 2	Density	0.263	1.635	0.405
	Entropy	-0.047	-0.075	-0.074
	Enthalpy	-0.061	-0.298	-0.096
	Cp	2.408	**17.018**	4.430
Table 3	Density	0.009	-0.296	0.016
	Entropy	-0.001	0.078	-0.003
	Enthalpy	-0.002	0.089	-0.004
	Cp	0.087	**1.584**	0.158

Additionally, Mach contours at the mid-plane and normal to the throat of the CD nozzle were investigated to determine the effect of modeling with the two tables of different resolution had on the resulting flow field. As observed for Case 2, there were noticeable differences in the contours attained through the use of Table 2 and 3, even more so in this case. This finding further concludes that the table resolution required to accurately represent sCO_2 thermodynamic properties greatly depends on the static conditions proximity to the saturation line.

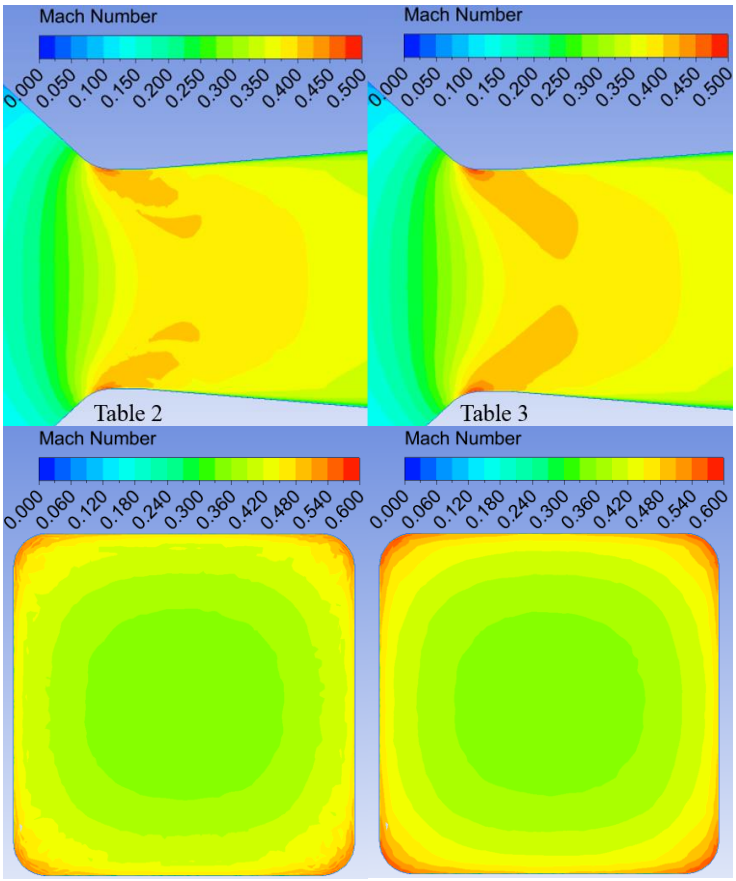

Figure 27: Mach Profiles through the CD Nozzle Mid-Plane (Top) and Normal to Throat (Bottom) using Table 2 (Left) and Table 3 (Right)

In order to investigate the possibility of utilized a RGP table that includes metastable properties to model past the saturation line, modeling of Case 3 was performed, where the throat conditions met the saturation line. Although the mass average reports at the throat displayed temperature and pressure values that were not surpassing the saturation line, to locally investigate cells that the metastable properties were applied to, iso-volumes were used. To first define the iso-volumes, cells were isolated in which met a certain pressure below the critical pressure. Then, REFPROP was used to determine the resulting saturation temperature at that pressure and further, temperature contours were implemented on the iso-volumes. This process enabled further examination of where cells proceeded below the saturation line. A select few contour images at

pressures of 7.0 MPa, 6.8 MPa, and 6 MPa can be seen in Figure 28, Figure 29, and Figure 30 respectively. When comparing the temperature contour range to the saturation temperature at that prescribed pressure, all iso-volumes display areas going below the saturation line within the throat, specifically around the corners.

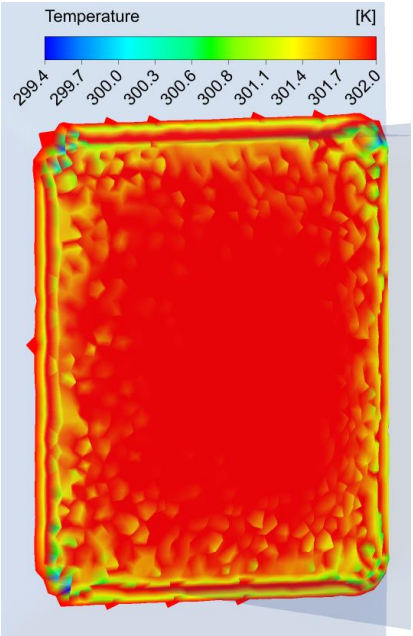

Figure 28: Iso-Volume Displaying Cells that meet Pressure of 7.0 MPa with Temperature Contour to Visualize Where Properties Are Below Saturation (Tsat = 301.833 K)

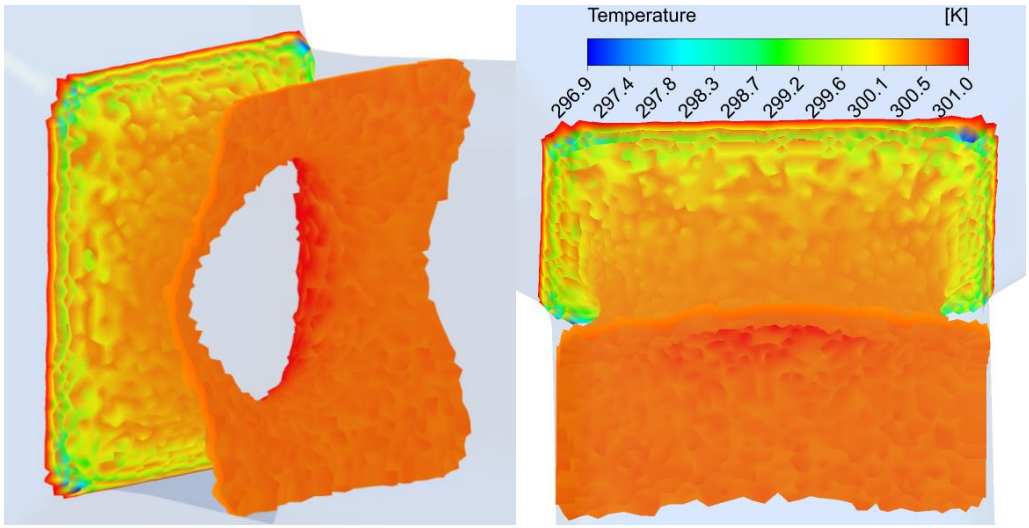

Figure 29: Iso-Volume Displaying Cells that meet Pressure of 6.8 MPa with Temperature Contour to Visualize Where Properties Are Below Saturation (T_{sat} = 300.563 K)

The iso-volume displaying all cells that meet a pressure of 6.8 MPa displays the largest amount of area where properties are in the two-phase zone (Figure 29) out of the three chosen pressures investigated.

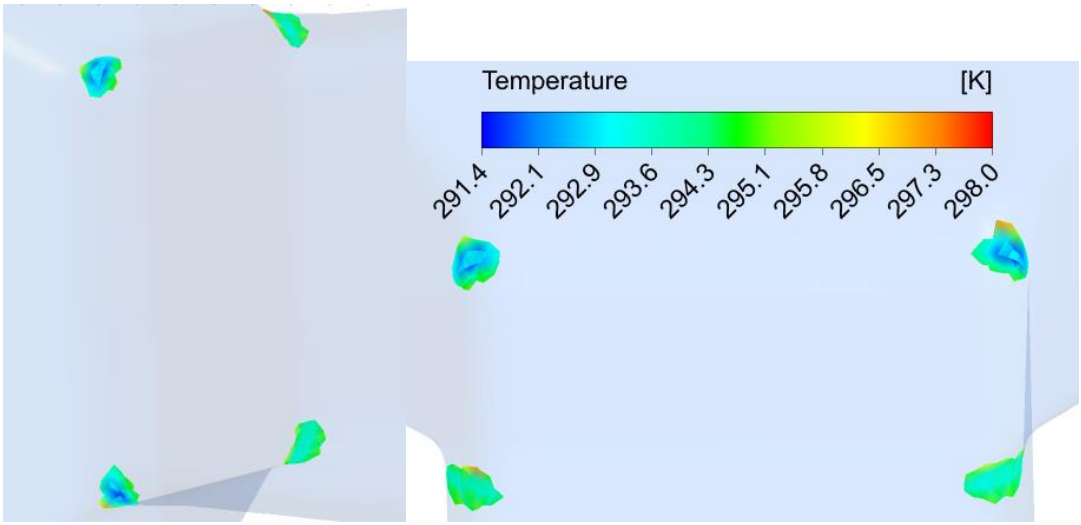

Figure 30: Iso-Volume Displaying Cells that meet Pressure of 6.0 MPa with Temperature Contour to Visualize Where Properties Are Below Saturation (T_{sat} = 295.128 K)

These results prove that modeling can be performed past the saturation line without the complexity of simulating two-phase flow. The accuracy of this method still needs to be assessed and the operating range in which this method will hold up needs to be determined further.

5.3 Chapter Summary

As industrial modeling capabilities are essential for the design and optimization of turbomachinery in sCO_2 power cycles, an option for decreasing the computational time and simplifying modeling when working with potential locations of metastable properties is investigated. The proposed option for modeling of sCO_2 compressors as well as other regions of possible two-phase flow, such as seals, was through utilizing a user defined two dimensional property table as the EOS. This option can further simplify the modeling processes by amending the real gas property table with metastable properties to enable single phase calculations within non-equilibrium phase change operation. The accuracy of the RGP table methodology is investigated through comparison of table interpolation error for tables with varying resolution. A converging-diverging nozzle is used to carry out this study that has geometrical similarity to the compressor analyzed in the previous chapter. Three distinct modeling cases are carried out in which the stagnation properties at the throat of the nozzle increasingly get closer to the saturation line and the critical point of the fluid. The Mach number is set so that two of the cases resulting static properties at the throat was just outside of the saturation dome and one was set so that the some of the static properties within the throat of the nozzle fall into the saturation dome, but do not exceed the spinodal limit. These cases are utilized to first understand the impact of the resolution of the tables on the accuracy of the results obtained and then to further understand the

use of the metastable properties and the additional modeling capabilities that come with using this method.

CHAPTER 6: CONCLUDING REMARKS AND FUTURE WORK

Throughout this research, 3D CFD and 1D analytical methods were utilized to carry out an analysis of a centrifugal compressor impeller designed to be employed in a large scale sCO_2 power cycle. The difficulties and unique considerations for the analytical methodologies that are brought about through the use of this unconventional gas was investigated. The limitation within 3D modeling through commercial CFD code, ANSYS Fluent are noted.

Due to the inability to model two phase flow within the chosen commercial solver, the boundary conditions have to be set so that property values do not surpass the saturation line within the impeller domain. These estimated boundary conditions are found through the mean line analysis of the impeller under investigation where a safety factor for the relative Mach number at the impeller inlet to the AMC Mach number is utilized to ensure that there is no two phase flow occurrence. To further ensure that the solving process was not abruptly stopped by reaching the saturation conditions, the limit for temperature and pressure were set far away from the critical point at the start of the modeling process. Next, these values were further decreased to values only slightly above the critical value for temperature and below the critical value for pressure when the simulation starts to stable. The converged solution still had cells that met the minimum temperature criteria but these were not of concern to the solution obtained due to the insignificant amount.

To understand the accuracy of using the option of creating a NIST real gas property table within Fluent, a comparison is performed between the mass average property values obtained through the CFD solution and the REFPROP exact calculated values for the inlet and the outlet of the impeller. This comparison displayed significant deviation in the interpolated property values to the exact value from REFPOP for a few select properties at the inlet to the impeller. Although

this option reduces the modeling computational time, due to the inability to control the resolution of the table, caution should be taken when defining the EOS through this method when working with inlet conditions close to the saturation line of the fluid.

An aerodynamic analysis of the selected compressor impeller is performed through the two analyses and a comparison of the results was carried out to determine where the results differ. The main differences observed were in the total pressure ratio, slip factor at the impeller exit, and the aerodynamic efficiency calculated. The aerodynamic efficiency predicted through the CFD analysis was lower while the total pressure ratio was higher than that obtained through the 1D analysis. Further, there was less slip observed within the CFD analysis, indicating that the resulting flow field was more guided by the blades than what was estimated by the 1D analysis. The difference in the two analyses may be accounted for by:

- Loss models used in mean line analysis code were developed through experiments with ideal fluids and thus do not account for the large fluctuations in fluid properties and the low compressibility factor when working with sCO_2.
- Limiting the temperature to ensure flow does not go into two phase in the CFD analysis may have impact on the results obtained, although few cells met the limiting temperature value.
- Utilizing the NIST real gas property table as the EOS led to interpolation error within certain properties that could have affected the results obtained.
- The compressor investigated was designed for a cycle with a net power output that was a magnitude greater than observed in past 1D and 3D analyses comparisons performed for

sCO_2 centrifugal compressors and thus many uncertainties reside in both of the analytical methodologies.

Currently, no experimental tests have been performed on sCO_2 compressors designed for large scale (100 MW) power cycles, as most are still designed for cycles that are in the kW range for power output in order to further understand instabilities and operational difficulties for this component. Due to the lack of experiments performed on large scale sCO_2 compressors, researchers have been focused on small scale compressors to validate CFD methodology due to the readily available experimental results to compare to. To the author's knowledge, this work serves as the first comparison of 1D and 3D CFD analyses methodology on a large scale sCO_2 compressor design. The compressor under investigation in this work was designed for a 100 MW sCO_2 power cycle, which is an order of magnitude in power higher than what has been investigated through CFD within literature. With this known, it is hard to determine the ambiguity between the two analyses along with their accuracy at predicting the compressor performance when sCO_2 is utilized. Additional experimental tests on this compressor would be needed to make any further conclusions.

To further the modeling capabilities, the effect of utilizing metastable and equilibrium temperature and pressure dependent real gas property tables within ANSYS CFX to model sCO_2 flow through a converging-diverging duct are assessed. The resolution of the tables was found to have a large impact on the flow field along with the accuracy of the results. Three tables were assessed with varying temperature and pressure resolutions. The required resolution of the table was determined to be dependent on the proximity of the stagnation properties to the critical point. This was assessed through comparing the stagnation temperature, pressure, and entropy at the

throat of the CD duct. Comparison of the results between the coarsest and the finest RGP tables displayed that as the operating conditions of the duct became closer to the critical values, the accuracy diminished and a finer table was required. Additionally, RGP tables that include metastable properties was determined to be a suitable option to further the modeling capabilities while still simulating single phase flow. Further investigation needs to be performed for examining condensation occurrence with properties closer to the critical point and further into the saturation dome.

Throughout this work, the reasons to why there are difficulties when modeling with sCO_2 were examined and further options to simplify this process were explored. Future work will investigate the application space of the defined metastable properties through experimental measures of a converging-diverging nozzle with high pressure sCO_2. The design process for this experiment is already under way and a schematic of the experimental set-up can be seen in Figure 31 in the Appendix. For this, shadowgraph and schlieren photography will be utilized to visualize the density change within the nozzle. Further measurements of pressure, temperature, and mass flow rate will allow comparison of experimental measurements to theoretical metastable calculated properties from REFPROP to validate the estimated metastable properties. Additional intent is to understand condensation phenomena through the fast acceleration of the flow for applications within turbomachinery such as the one discussed within this paper as well as flow through seals and disk clearances. Future work will also serve as a process to develop best practices for flow visualization when working with high pressure sCO_2.

APPENDIX: FUTURE SCO2 FLOW EXPERIMENT SCHEMATIC

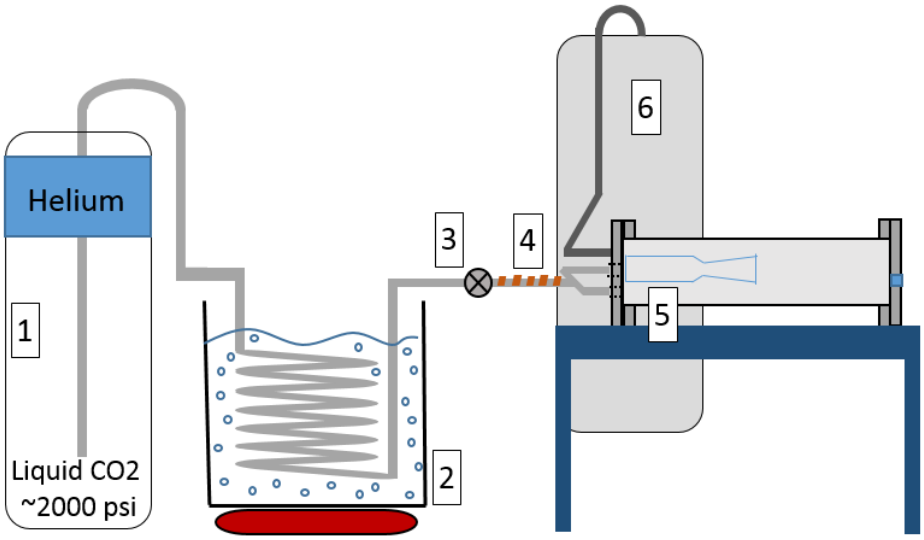

Figure 31: sCO2 Flow through Converging-Diverging Duct Experiment Set up Schematic

Table 17: Location Descriptions for sCO2 Flow Experiment

Location	Description
1	sCO2 Helium Head Padded Supply Cylinder
2	Heated Water Bath
3	sCO2 High Pressure Regulator
4	Heating Tapes
5	Converging-Diverging Test Section and Pressure Vessel
6	sCO2 Exhaust Tank

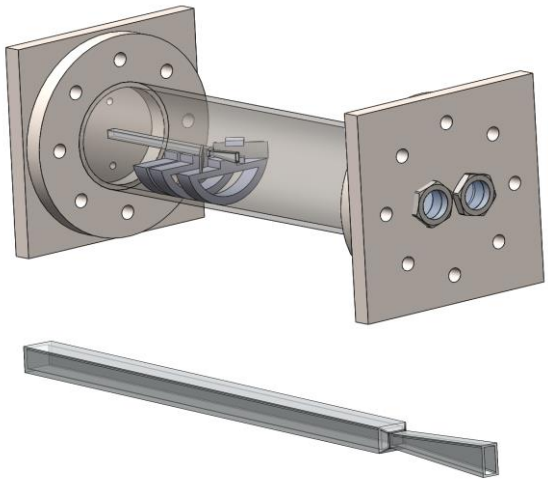

Figure 32: Test Section and Surrounding Components with Visible Sight Windows

REFERENCE

[1] "Energy and Air Pollution, World Energy Outlook," International Energy Agency, Paris, France, 2016.

[2] "World Energy Outlook 2015 Executive Summary," International Energy Agency, Paris, France, 2015.

[3] Energy Information Agency, "Annual Energy Outlook 2016," US Department of Energy, Washington, DC , 2016.

[4] V. Dostal, "A Supercritical Carbon Dioxide cycle for the Next Generation Nuclear Reactors," Department of Nuclear Engineering, Massachusetts Institute of Technology, Boston, Massachusetts, 2004.

[5] V. Dostal, P. Hejzlar and M. J. Driscoll, "High Performance Supercritical Carbon Dioxide Cycle for Next-Generation Nuclear Reactors," *Nuclear Reactors,* vol. 154, no. June, 2006.

[6] H. Douglas, "Phase Approach to Development of a High Temperature sCO2 Power Cycle Pilot Test Facility," in *The 5th International Supercritical CO2 Power Cycles Symposium*, San Antonio, TX, 2016.

[7] M. L. Bauer, R. Vijaykumar, M. Lausten and J. Stekli, "Pathways to Cost Competitive Concentrated Solar Power Incorporating Supercritical Carbon Dioxide Power Cycles," in *The 5th International Supercritical CO2 Power Cycles Symposium*, San Antonio, TX, 2016.

[8] C. Lettieri, D. Yang and Z. Spakovszky, "An Investigation of Condensation Effects In Supercritical Carbon Dioxide Compressors," *ASME Journal of Engineering for Gas Turbines and Power,* vol. 137, no. August, 2015.

[9] J. Starzmann and M. V. Casey, "Non-equilibrium Condensation Effects on the Flow Field and the Performance of Low Pressure Steam Turbine," in *ASME Turbo Expo*, Glasgow, UK, 2010.

[10] E. Rinaldi, R. Pecnik and P. Colonna, "Steady State CFD Investigation of a Radial Compressor Operating with Supercritical CO2," in *ASME Turbo Expo,* San Antonio, TX, 2013.

[11] J. Schmitt, R. Willis, D. Amos, J. Kapat and C. Custer, "Study of a Supercritical CO2 Turbine with TIT of 1350 K for Brayton Cycle with 100 MW Class Output: Aerodynamic Analysis of Stage 1 Vane," in *ASME Turbo Expo*, Dusseldorf, Germany, June, 2014.

[12] J. Qi, T. Reddell, K. Qin, K. Hooman and I. H. J. Jahn, "Supercritical CO2 Radial Turbine Design Performance as a Function of Turbine Size Parameters," in *ASME Turbo Expo*, Seoul, South Korea, 2016.

[13] R. L. Fuller and K. Eisemann, "Centrifugal Compressor Off-Design Performance for Super-Critical CO2," in *The Supercritical CO2 Power Cycle Symposium*, Boulder, CO, 2011.

[14] S. A. Wright, R. F. Radel, M. E. Vernon, G. E. Rochau and P. S. Pickard, "Operation and Analysis of a Supercritical CO2 Brayton Cycle," Sandia National Laboratory, Albuquerque, NM; Livermore, CA, 2010.

[15] B. M. Brenes, "Design of Supercritical Carbon Dioxide Centrifugal Compressors," Ph.D. Dissertation, Group of Machines and Motors of Seville, University of Seville, Seville, Spain, 2014.

[16] R. B. Vilim, "A One-Dimensional Compressor Model for Super-Critical Carbon Dioxide Applications," in *International Congress on Advances in Nuclear Power Plants*, San Diego, CA, June 13-17, 2010.

[17] S. S. Sanghera, "Centrifugal Compressor Meanline Design Using Real Gas Properties," Carleton University, Ottawa, Ontario, Canada, 2013.

[18] H. W. Oh, E. S. Yoon and M. K. Chung, "An Optimum Set of Loss Models for Performance Prediction of Centrifugal Compressors," *Proceedings of the Institution of Mechanical Engineers*, vol. 211, no. Part A, pp. 331-338, 16 April 1997.

[19] R. A. Bidkar, A. Mann, R. Singh, E. Sevincer, S. Cich, M. Day, C. D. Kulhanek, A. M. Thatte, A. M. Peter, D. Hofer and J. Moore, "Conceptual Design of 50 MWe and 450 MWe Supercritical CO2 Turbomachinery Trains for Power Generation from Coal.Part 1: Cycle and Turbine," in *The 5th International Symposium - Supercritical CO2 Power Cycles* , San Antonio, TX, 2016.

[20] R. A. Bidkar, G. Musgrove, M. Day, C. D. Kulhanek, T. Allison, A. M. Peter, D. Hofer and J. Moore, "Conceptual Design of 50 MWe and 450 MWe Supercritical CO2 Turbomachinery Trains for Power Generation from Coal.Part 2: Compressors," in *The 5th International Symposium - Supercritical CO2 Power Cycles* , San Antonio, TX, 2016.

[21] E. Rinaldi, R. Pecnik and P. Colonna, "Computational fluid Dynamic Simulation of a Supercritical CO2 Compressor Performance Map," *ASME Journal of Engineering for Gas Turbines and Power,* vol. 137, July 2015.

[22] R. Pecnik, E. Rinaldi and P. Colonna, "Computational Fluid Dynamics of a Radial Compressor Operating With Supercritical CO2," *ASME Journal of Engineering for Gas Turbines and Power* , vol. 134, no. 12, 2012.

[23] R. Span and W. Wagner, "A New Equation of State for Carbon Dioxide Covering the Fluid Region from the Triple-Point Temperature to 1100 K at Pressures up to 800 MPa," *Journal of Physical and Chemical Reference Data,* vol. 25, pp. 1509-1596, 1996.

[24] B. I. Lee and M. G. Kesler, "A Generalized Thermodynamic Correlation Based on Three-Parameter Corresponding States," *American Institute of Chemical Engineering,* vol. 21, no. 3, pp. 510-527, 1975.

[25] N. D. Baltadjiev, "An Investigation of Real Gas Effects in Supercritical CO2 Compressors," Massachusetts Institute of Technology, Cambridge, MA, 2012.

[26] E. W. Lemmon, M. L. Huber and M. O. McLinden, *NIST Standard Reference Database 23, Reference Fluid Thermodynamic and Transport Properties - REFPROP,* Ver. 9.1 ed., Gaithersburg, MD: National Institute of Standards and Technology, Standard Reference Data Program, 2013.

[27] B. Monje, D. Sanchez, R. Chacartegui, T. Sanchez, M. Savill and P. Pilidis, "Aerodynamic analysis of Conical Diffusers Operating with Air and Supercritical Carbon Dioxide," *International Journal of Heat and Fluid Flow,* no. 44, pp. 542-553, 2013.

[28] N. D. Baltadjiev, C. Lettieri and Z. S. Spakovszky, "An Investigation of Real Gas Effects in Supercritical CO2 Centrifugal Compressors," *ASME Journal of Turbomachinery,* vol. 137, no. September, 2015.

[29] ANSYS Academic Research, "Release 14.5, Theory Manual," ANSYS Inc., Canonsburg, PA.

[30] D. Paxson, C. Lettieri, Z. Spakovszky, P. Bryanston-Cross and A. Nakaniwa, "Experimental Assessment of Thermodynamic Properties of Metastable CO2," in *The 5th International Symposium - Supercritical CO2 Power Cycles,* San Antonio, TX, 2016.

[31] Y. Gong, N. A. Carstens, M. J. Driscoll and I. A. Matthews, "Analysis of Radial Compressor Options for Supercritical CO2 Power Conversion Cycles," MIT Gas Turbine

Laboratory of the Department of Aeronautics and Astronautics , Cambridge, MA, 2006.

[32] A. Ameli, T. Turunen-Saaresti and J. Backman, "Numerical Investigation of the Flow Behavior Inside Supercritical CO2 Centrifugal Compressors," in *ASME Turbo Expo*, Seoul, South Korea, 2016.

[33] T. A. Munroe, M. A. Zaccaria, W. H. Flaspohler, R. J. Pelton, K. D. Wygant and O. B. Dubitsky, "FLUENT CFD Steady State Predictions of a Single State Centrifugal Compressor with Supercritical CO2 Working Fluid," in *The Supercritical CO2 Power Cycle Symposium*, Troy, NY, April, 2009.

[34] L. Blanchette, A. Khadse, M. Mohagheghi and J. Kapat, "Two Types of Analytical Methods for a Centrifugal Compressor Impeller for Supercritical CO2 Power Cycles," in *AIAA Propulsion and Energy Forum*, Salt Lake City, UT, 2016.

[35] M. Mohagheghi and J. Kapat, "Pareto Based Multi-Objective Optimization of Recuperated S-CO2 Brayton Cycles," in *ASME Turbo Expo*, Dusseldorf, Germany, 2014.

[36] M. Mohagheghi, H. Zawati, T. Pinol, J. Gou, C. Xu and J. Kapat, "Use of 1-D Finite Enthalpy Method for a High-Temperature Recuperator Made of Polymer Derived Ceramic Composite for a Supercritical Carbon Dioxide Power System," in *The 5th International Symposium - Supercritical CO2 Power Cycles*, San Antonio, TX, March, 2016.

[37] R. H. Aungier, Centrifugal Compressors: A Strategy for Aerodynamic Design and Analysis, New York: ASME Press, 2000.

[38] W. Jansen, "A Method for Calculating the Flow in a Centrifugal Impeller when Entropy Gradients are Present," in *Royal Society Conference on Internal Aerodynamics (Turbomachinery)*, 1967.

[39] F. J. Wiesner, "A Review of Slip Factors for Centrifugal Impellers," *ASME Journal of Engineering for Power*, vol. 89, pp. 558-572, 1967.

[40] I. ANSYS, "ANSYS Fluent Theory Guide," SAS IP, Inc., Canonsburg,Pa, 2013.

[41] I. B. Celik, U. Ghia, P. J. Roache, C. J. Freitas, H. Coleman and P. E. Raad, "Procedure for Estimation and Reporting of Uncertainty Due to Discretization in CFD Applications," *Journal of Fluids Engineering*, vol. 130, no. 7, 2008.

[42] E. Lemmon, "Answers to Frequently Asked Questions," NIST, 24 October 2016. [Online]. Available: http://www.boulder.nist.gov/div838/theory/refprop/Frequently_asked_questions.htm#FLSRoutinesandMetastableStates. [Accessed 27 October 2016].

[43] H. Schlichting, Boundary-Layer Theory, 7th ed., New York: McGraw-Hill, 1979, pp. 145-156.